ABSTRACT

Title of Document:	MINIATURE FIBER OPTIC PRESSURE SENSORS FOR INTERVERTEBRAL DISC PRESSURE MEASUREMENTS IN RODENTS
	Silas Nesson, M.S., 2007
Directed By:	Assistant Professor Miao Yu, Department of Mechanical Engineering

Mechanical stress due to interstitial fluid pressures can play a major role in the development of disc degeneration, a common cause of lower back pain. Pressures generated in the intervertebral disc have previously been measured in humans and animals. However, due to their small size, thus far it has been difficult to experimentally measure pressures in rodents. With the prevalent use of rodent disc models in mechanobiology, it is important to characterize the intradiscal pressures under externally applied stresses. In this thesis research, two different optical systems with novel miniature fiber optic pressure sensors have been developed. These systems are an intensity based solid-tip sensor system and a low coherence Fabry-Perot sensor system. Pressure sensors, which have diameters of only 363 µm, were designed to measure pressures in rat discs without disrupting the structure and altering the intradiscal pressures. For the first time, *in vitro* intradiscal pressure measurements of rodents have been successfully demonstrated by using these sensors.

MINIATURE FIBER OPTIC PRESSURE SENSORS FOR INTERVERTEBRAL
DISC PRESSURE MEASUREMENTS IN RODENTS

By

Silas Nesson

Thesis submitted to the Faculty of the Graduate School of the
University of Maryland, College Park, in partial fulfillment
of the requirements for the degree of
Master of Science
2007

Advisory Committee:

Assistant Professor Miao Yu, Chair, Department of Mechanical Engineering

Professor Balakumar Balachandran, Department of Mechanical Engineering

Assistant Professor Adam Hsieh, Department of Bioengineering

Dedication

This thesis is dedicated to my family for their continuous support and encouragement, and to my friends, some of whom would relentlessly make sure I was hard at work, and others who would persistently distract and entertain me.

Acknowledgements

I would like to express my sincere appreciation to my research advisor, Professor Miao Yu, for her constant guidance and encouragement. Her support during the course of my research was an invaluable asset, and I could not have completed it without her.

I would also like to thank Professor Balakumar Balachandran, not only for being on my thesis committee, but also for his guidance and advice. Thanks to Professor Adam Hsieh for his invaluable contributions to my research, his constant aid when I was in need, and for being on my committee.

I am grateful to my lab mates Zhong Chen and Yuxiang Liu for their mentoring, selfless assistance, and the occasional snacks. I am also thankful to those that helped me from the Bioengineering Department, including Dave Ryan, Adam Gabai, Alvin Yew, Hyunchul Kim, and others.

I wish to express my special thanks to my graduate school friends Sasha Tsarev, Damien Bretall, Rifat Jafreen, Chrissy Ikeda, Adam Gabai, Jason Smoker, and the German gang of both past and present, all of whom have given me an unforgettable graduate school experience.

Finally, I would like to thank all my other friends and family for their endless support and encouragement.

Table of Contents

List of Figures

Chapter 1: Introduction

1.1 Motivation

Due to its common occurrence with aging and its ability to manifest itself as a clinically debilitating back pain, degenerative disc disease continues to pose major health concerns in people [1,2]. With the identification of risk factors such as genetics, nutrient supply, and mechanical stress, it becomes necessary to determine what role each of these risk factors plays in degeneration at the cellular and molecular levels. Previously conducted studies with rodents have demonstrated that depending upon the applied loading, the mechanical compressive stress can be beneficial or detrimental to the disc health. However, it is still unclear as to what physical mechanisms cause these different disc responses in rodents, and whether these mechanisms can be related to human responses. Further study on linking rodent disc degeneration to those in humans is critical for the future development of preventive measures against human disc disease.

One aspect of stress that has been demonstrated to affect disc cell biology is interstitial fluid pressure, which refers to the fluid inside the nucleus pulposus. A histology and schematic of an intervertebral disc is shown in Figure 1.1. Measuring pressure within the nucleus experimentally in rodent tail discs would not only provide a tool for directly linking transient pressure effects with cellular response, but it would also enable comparisons of load-induced pressure changes in rodents with those measured in humans. Verifying the relevance of these intradiscal pressure-external load relationships in rats would lend further support to the appropriateness of

in vivo rodent tail disc loading models for studying the mechanisms of disc degeneration.
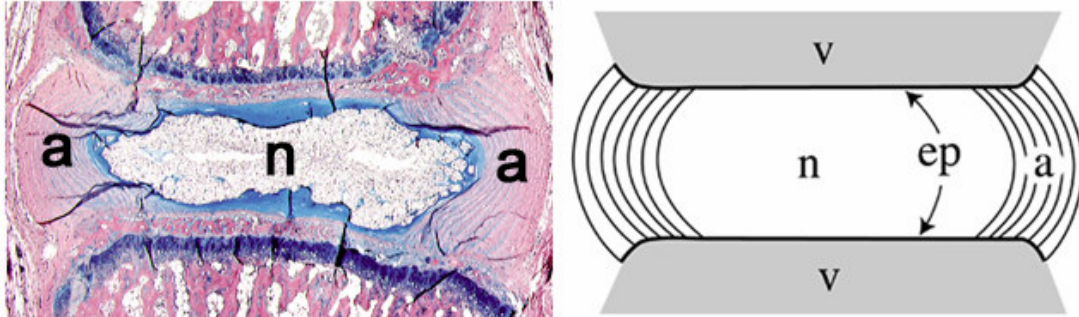
Figure 1.1: Histology and schematic of a healthy intervertebral disc, illustrating the vertebrae (**v**), endplates (**ep**), nucleus (**n**), and annulus (**a**) [3].

A major step toward future work would be to validate the internal mechanics of healthy and degenerate rodent tail discs by measuring intradiscal pressures within the nucleus at varying loads and conditions. It is hypothesized that by virtue of similar intradiscal pressure-external load relationships, rodent tail discs are valid biomechanical analogues of human discs. To test this hypothesis, a miniature pressure sensor that can be safely inserted into the rat disc through the annulus fibrosus is required. However, this is a limitation that currently commercially available sensors cannot overcome. An intradiscal pressure study in rodents will have a direct impact on characterizing the physical and molecular mechanisms involved in load-induced disc degeneration. Specifically, measuring rat intradiscal pressures will allow for validating current computational models, identifying pressures that are relevant for *in vitro* cell culture stimulation for rodent tissues, and bridging events observed in rodent disc models to applications in human discs. This thesis study

involves the development and implementation of novel sensor devices with established approaches to obtain such previously inaccessible data.

Commercially available miniature sensors have already been used to measure pressures in human, porcine, and rabbit discs [1-6]. In intradiscal pressure measurements, a miniature sensor is traditionally inserted through the annulus into the nucleus by way of a small needle. However, even these small diameter probes are too large or have an inappropriate shape to be inserted into rodent discs without altering disc mechanics. Due to the dimensions of the rodent disc, which is only a few millimeters in height, it is necessary to verify the size of the pressure sensor that can be used without causing any disruptions. Research has been conducted by Hsieh and Ryan to validate that annular puncture of the disc of certain sizes does not adversely affect the rodent disc mechanics [7]. The annulus, otherwise known as the outer wall of the intervertebral disc, has a large contribution to intradiscal pressures and must be kept in tact. Since the hypodermic needle is used to puncture the annulus to feed a pressure sensor into the rodent disc, this study examined the effects of various sizes of hypodermic needles on the overall disc mechanics to determine the maximum allowable size that would not cause any irreparable damage. Experimental results obtained from their study showed that the insertion of a 22 gauge needle or smaller to introduce the pressure sensor into the disc would not adversely affect the disc mechanics; this prescribes an approximate maximum diameter of 400 µm for the pressure sensor.

The development of a sensor system for intradiscal pressure measurements is challenging because of the following: i) the sensor must have a miniature size with a

maximum diameter of 400 µm and ii) there is a lack of sufficient understanding on the required sensitivity, dynamic range, and resolution of the sensor.

Recent technological breakthroughs in fiber optic sensors have enabled the development of sensors small enough to insert directly into rat discs through the annulus fibrosus without causing adverse effects to disc mechanics. In addition to their inherent small size, fiber optic sensors have the advantages of being light weight, biocompatible, highly sensitive, and not susceptible to electromagnetic interference (EMI) [8]. Optical sensors can also be exceedingly versatile, making it an appropriate choice for rodent disc pressure measurements. In this work, fiber optic sensor systems with novel miniature pressure sensors are developed to fulfill the requirements of intradiscal pressure measurements in rat discs.

1.2 Literature Review

1.2.1 Previous Studies on Intradiscal Pressure Testing

There have been many studies in which intradiscal pressures have been measured in humans as well as animals using miniature pressure transducers. In these studies, pressures are measured by a sensor varying from 0.55 mm to 1.7 mm in diameter and the sensor is generally inserted into the disc via a puncture produced by a probe or hypodermic needle.

Edwards *et al*. [1] measured *in vitro* pressures within cadaveric lumbar intervertebral discs in humans to examine the distribution of stress across the area of the disc and compare regional variations in peak stress during compression loading. In this research, a pressure transducer was embedded into a 16 gauge needle with a pointed tip to facilitate positioning within the disc. The needle itself was 1.7 mm in

diameter, with the pressure transducer embedded approximately 4.5 mm from the pointed tip. An x-y table was used for positioning the probe to be inserted from anterior to posterior through the spine specimen, which was vertically mounted. Test results showed that the highest pressure values were measured during extension/compression within the annulus, corresponding to common sites of disc degeneration and herniation.

Wilke *et al*. [2] conducted *in vivo* intervertebral disc pressure tests in the lumbar vertebrae of a human to provide a database of pressure measurements together with anthropometric data as a basis for a model that predicts spinal loads. A flexible pressure transducer with a 1.5 mm diameter was implanted into the nucleus pulposus of the healthiest disc of a volunteer. Pressure values were recorded during various postures, activities, and exercises such as lifting activities, sitting unsupported on a stool or an ergonomic sitting ball, and body lifting by arm supports.

Polga *et al*. [4] measured *in vivo* pressures in thoracic discs in 6 human volunteers to quantify and compare pressure from the middle and lower thoracic spine during various positions and maneuvers, as well as to investigate the variations of pressures based on the transducer's orientation. The pressure transducer was inserted into the center of the disc by first puncturing it with a guide needle, inserting a guide tube over the needle, then removing the needle, and threading the 1.3 mm diameter transducer through the tube. Experiments proved that thoracic intradiscal pressure varied significantly with different body positions and maneuvers but not disc level. Additionally, the measurements showed that in some positions, thoracic disc

pressures were significantly different from previously reported pressures from lumbar spine discs.

Intradiscal pressure tests in animals with smaller discs have also been conducted. Guehring *et al*. [5] measured *in vivo* intervertebral disc pressures in the lumbar spine of rabbits to determine how temporary external disc compression and distraction were associated with pressure changes. A commercial fiber optic pressure sensor was used, and to insert the sensor, an 18 gauge needle horizontally punctured the disc and then was withdrawn and simultaneously replaced by the sensor. The experiments supported that temporary compression leads to moderate disc degeneration, and proved fiber optic sensing was an accurate method of evaluating disc status without injuring the disc significantly.

Again by using a commercial fiber optic pressure sensor, *in vivo* porcine intradiscal pressure experiments were conducted by Ekström, Holm, Holm, and Hansson [6] to establish the relationship between the disc pressure in the nucleus and the load applied to the motion segment. The fiber optic pressure sensor used to measure the pressures has a diameter of 0.55 mm. A 20 gauge needle was inserted through the lateral part of the disc into the central nucleus pulposus, after which the sensor was passed fully through the needle into the nucleus and the needle was retracted. Intradiscal nucleus pressure was found to be rather linearly dependent on the applied load and pressure measurement results also indicated that the disc exhibited a creep behavior.

1.2.2 Previous Work on Miniature Fiber Optic Pressure Sensors

The current state-of-the-art miniature optical pressure sensors consist mostly of fiber tip based Fabry-Perot sensors. This type of sensor, which contains a cavity formed between the fiber tip and a diaphragm surface, has shown promise in carrying out pressure measurements while still maintaining a small size. With currently practiced micro-fabrication techniques, it is possible to not only tailor a sensor to have the sensitivity, resolution, and dynamic range required for measuring intradiscal pressures in rodents, but also to manufacture sensors small enough to be inserted into rat discs without any adverse effects.

Wang *et al*. [9,10] have developed an optical fiber tip pressure sensor for medical diagnostics such as blood or intracranial pressure measurements. The sensor was fabricated by first splicing an optical fiber to a hollow fiber, which is then spliced to a small segment of another cleaved optical fiber acting as a diaphragm. Thus, a Fabry-Perot cavity was produced between the first fiber tip and the diaphragm. The sensor was employed in a fiber optic interferometer system consisting of a laser diode and a photodetector. It was demonstrated that the sensor responded well to pressure variations between 20 psi and 30 psi and it also showed good linearity and minimal hysteresis. It should be pointed out that as a miniature yet robust pressure sensing device, this sensor has many desirable attributes such as biocompatibility, a small diameter of only 125 µm, low cost, and disposability. However, splicing and cleaving such small segments of optical fibers is difficult to control and shape distortion, imperfect edges, and device non-uniformity are sometimes inevitable.

In another study, Zhu and Wang [11] developed a fiber tip pressure sensor by using a similar technique that only involves fusion splicing, cleaving, and etching. Instead of using a segment of hollow fiber, the sensor was made of commercial solid core silica fibers only, resulting in excellent mechanical properties that can withstand high temperature environments. The design utilizes a Fabry-Perot cavity produced by splicing different multimode fibers of varying doping substances to the fiber end and using wet chemical etching to create a cavity, finally splicing and cleaving another fiber to the end to produce a pressure sensitive diaphragm. A low coherence (white light) fiber optic system was used. This system consists of a light emitting diode (LED) source and an optical spectrum analyzer (OSA) to demodulate the sensor signal. The sensor was proven to work in the pressure range between 20 psi and 200 psi and survive in temperatures ranging up to 500º C. However, once again, the aforementioned problems associated with the fabrication process still exist.

Many other materials have also been utilized as pressure transducers. In a recent study, Totsu, Haga, and Esashi developed a pressure sensor that utilizes white light interferometry to measure the dynamic pressure changes in a goat heart [12,13]. The system utilizes a white light source in conjunction with a high speed spectrometer to measure the pressure induced deformations of a micro-electro-mechanical system (MEMS) diaphragm attached to a fiber end. The sensing element, produced mostly from SiO_2 and made reflective with an aluminum coating, is batch fabricated to allow for multiple potential sensors with identical properties. Although the MEMS fabricated diaphragm allows for mass production at a low cost, an exceedingly complex bonding process is necessary to attach the sensing element to an

optical fiber with a previously coated chromium half-mirror. This hinders the potential of the sensor to become a batch fabricated, disposable miniature blood pressure sensor. The resulting pressure sensor is of the same size as an optical fiber, which was proven to have good accuracy and linearity in the pressure range of -2 psi to 8 psi. Dynamic pressure measurements were demonstrated in the aorta and left ventricle of a goat.

Another fiber optic pressure sensor, which was developed by MacPherson, Kilpatrick, Barton, and Jones [14], also employs a diaphragm and this sensor was used in turbomachinery applications. A slightly modified Zirconia ferrule commonly used for fiber optic connectors was utilized to house the fiber. This ferrule contains a hole closely toleranced to match the dimensions of a standard fiber. At the end of the ferrule, a thin elastic diaphragm made from copper was constructed. The resulting sensor was less than 1 mm in diameter with an approximate 3 µm-thick diaphragm, where the diaphragm thickness can be altered during fabrication depending on the pressure range of the application. A laser diode and a photo detector were used in the optical interrogation system to determine optical phase changes during aerodynamic pressure measurements. However, this design showed some potential drawbacks associated with temperature sensitivity due to the different materials utilized and variations of their thermal and mechanical properties.

Many research groups have also reported miniature fiber optic pressure sensors with polymer diaphragms. A polymer has a lower elastic modulus than silicon and thus it experiences greater deflection to a given pressure, rendering a higher sensitivity as a pressure transducer. For example, Melamud *et al*. utilized an

SU-8 cap that fits onto the end of an optical fiber as the sensing element [15]. SU-8 is an epoxy-based photoresist that when cured, becomes glassy and biocompatible. By using standard photolithography techniques, a sensor cap with a diameter of approximately 300 µm was fabricated and glued onto the fiber end. The optical system utilized a broadband source and an OSA to demodulate the signal. Experiments conducted by using the sensor showed a linear response and satisfactory resolution for intravascular blood pressure measurements. However, undesired signs of swelling and sensitivity to temperature variation were also observed.

Cibula, Donlagic, and Stropnik [16] developed a miniature fiber optic pressure sensor that utilized a reflecting polymer diaphragm as a pressure transducer while still maintaining a 125 µm diameter. The optical system also utilized a LED light source and an OSA to demodulate the sensor signal. An elastic polymer in dimethyl formamide (DMF) was used to create a thin diaphragm by allowing it to creep into a cavity at the end of the fiber. Unfortunately, this fabrication is highly dependent on the DMF concentration and is hardy be repeatable.

In another work, Olson [17] designed a miniature fiber optic pressure sensor that was sensitive enough for intracochlear acoustic pressure measurements. The sensor utilized a thin polymer diaphragm as the pressure transducer. To create the diaphragm, a liquid drop of photosensitive polymer was dropped onto the surface of water where it expanded to a thin film. After a short pre-cure time, the thin film was attached onto the end of a glass capillary tube. Upon post curing, a gold layer was evaporated onto the polymer diaphragm to enhance the reflectivity and the performance of the sensor. An intensity based fiber optic sensing system was used to

measure the pressure induced diaphragm deflection. While the optical sensing system is rather basic, the sensor design allows for relatively easy, low cost, and repeatable sensor fabrication.

Study of these miniature fiber optic pressure sensor designs has provided great insight into possible systems and sensor designs for a miniature fiber optic sensor capable of measuring intradiscal pressures in rodents.

1.3 Objectives and Scope of Thesis Work

An overall objective of this thesis research is to design, develop, and study miniature fiber optic pressure sensor systems for intradiscal pressure measurements of rodents. Specific objectives of this thesis work are as follows:

i) Achieve an understanding of various fiber optical sensing strategies for pressure measurements and develop feasible fiber optic sensing systems for intradiscal pressure measurements in rodents

ii) design and develop miniature pressure sensing components capable of intradiscal pressure measurements without disruption to the disc structure

iii) demonstrate and validate intradiscal pressure measurements of rodents by using the developed sensor systems.

1.4 Thesis Organization

In this research, two different types of optical sensing systems and miniature pressure sensors have been developed and utilized in intervertebral disc pressure experiments. In Chapter 2, different optical sensor system configurations are reviewed and two different types of fiber optic sensor systems developed for

intradiscal pressure measurements are introduced. In Chapter 3, two types of miniature pressure sensor devices are designed, developed, and fabricated. In Chapter 4, experimental studies of the developed sensor systems are presented. These studies include *in vitro* intradiscal pressure measurements and sensor performance characterization. Conclusions, contributions of this thesis research, and suggestions for future work are collected together and provided in Chapter 5.

Chapter 2: Optical System Development

In this chapter, two types of fiber optic sensor systems are reviewed and the development of two different optical systems, one based on intensity measurements and another based on optical phase measurements, are presented and discussed.

2.1 Overview of Fiber Optic Sensor Systems

Fiber optic sensors are versatile and have been proven to be useful for a wide range of applications [18-20]. One of the many advantages of these sensors is that light transferred through optical fibers can be characterized by many different parameters including wavelength, intensity, phase, and polarization. Different choices of detection parameters allow for many different possible sensing mechanisms, which permits one to design fiber optic sensors for a wide variety of measurands in many different types of applications. In particular, for pressure sensors that are of interest to this thesis work, different possible designs have been explored for a wide range of applications [21,22].

Since fiber optic sensors are better suited than conventional mechanical or electrical sensors in situations involving high temperatures, high pressures, small spaces, and delicate environments such as biological tissues, these sensors open up avenues for many unconventional applications. In this research, a sensor is to be inserted into a rodent's tail to measure the pressure magnitude and variation within the disc between the vertebrae. This rodent disc pressure sensing application requires a sensor with the following attributes: i) the sensor size needs to be small enough (less than 400 µm in diameter) so that it will not disturb the structure and allow for

accurate *in situ* measurements, ii) the sensor needs to be biocompatible, and iii) the sensor needs be highly reliable, and iv) the sensor needs to have high resolution. A fiber optic sensor is an ideal choice for this application, since it can be miniaturized as well as designed to have the attributes mentioned above.

Among the aforementioned choices of detection parameters, two commonly used versions of fiber optic sensors are intensity based sensor systems and interferometry based sensor systems. Intensity based sensor systems make use of the change in light intensity to sense a physical quantity of interest, while interferometry based sensor systems make use of the change in the optical phase to sense a physical quantity of interest. The basic principles of the intensity and interferometry based sensing systems are explained in the next two sections.

2.1.1 Intensity Based Fiber Optic Sensor System

An intensity based sensor system, also referred to as an intensity or amplitude modulated sensor system, is one of the earliest forms of optical sensing due to its simple nature. Intensity based sensor systems have the following advantages: i) inherent simplicity, ii) reliability, iii) ease of implementation and use, and iv) low cost. However, an intensity based sensor system usually has relatively low sensitivity, a small dynamic range, and is also susceptible to light source power fluctuations and various other disturbances.

In general, in an intensity based sensor system, light from a source is used to illuminate a fiber optic sensor where it reacts to some form of disturbance. The light beam exiting the sensor is received by a photodetector or a power meter, and on occasion, an electronic processing unit as well. The light beam propagating through

the optical sensor is modulated either directly by the disturbance or through a disturbance induced optical propagation length change in the fiber itself. In either case, the intensity change detected by the sensor system is directly related to a variation of the physical quantity of interest. Ideally, this change in intensity should be linearly proportional to the measurand. This type of system is commonly used to sense physical parameters such as force, pressure, displacement, and acceleration as well as other quantities such as electrical, chemical, magnetic, or thermal quantities.

Intensity based sensors can have many different configurations, but one common configuration that is widely used is the transmission gap or fiber loss configuration, in which there is a gap between an input fiber and an output fiber [23]. A schematic of this configuration is shown in Figure 2.1. In this arrangement, there is a light source, two optical fibers that are held in line in close proximity of each other, and a detector to measure the transmitted light intensity. Light coupled from the source into the left fiber (transmitting fiber) travels with minimal loss until it reaches the transmission gap. Due to diffraction, light exiting the left fiber at the gap expands. The exiting angle is the same as the acceptance angle of the fiber, which depends on the difference between the refraction index of the core and that of the cladding of the optical fiber. The amount of light captured by the right fiber (receiving fiber) depends on its acceptance angle and the axial separation z between the optical fibers. When the separation z is modulated, it in turn results in an intensity modulation of the light captured [24].
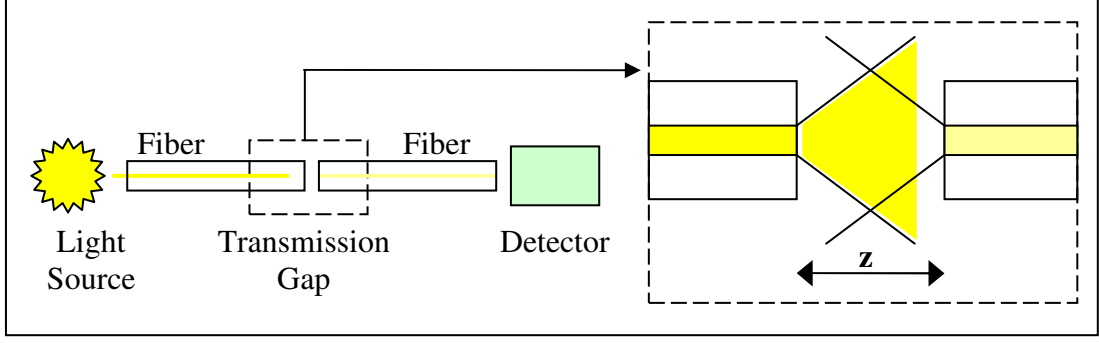
Figure 2.1: Schematic of an intensity based sensor system with a transmission gap.

As light propagates through the transmission gap, the spot size $w(z)$ as a function of the gap distance z can be expressed as [20]

$$w(z) = w_0 \sqrt{1 + \left(\frac{z\lambda}{\pi w_0} \right)^2} \quad , \tag{2.1}$$

where w_0 is the initial spot size (beam waist) when the light beam exits the transmitting fiber, and λ is the center wavelength of the light. The subsequent intensity profile of the light can be expressed as

$$I(\rho, z) = I_0 \left(\frac{w(z)}{w_0} \right)^2 e^{-2\frac{\rho^2}{w^2(z)}} \quad , \tag{2.2}$$

where ρ is the radial distance from the optical axis. When the light is just exiting the transmitting fiber, the intensity profile can be described as

$$I(\rho, 0) = I_0 e^{-2\frac{\rho^2}{w_0^2}} \quad . \tag{2.3}$$

A portion of the transmitted light propagating through the gap is captured by the core of the receiving fiber and then travels through to the detector, where a measurement of intensity or power is made. The amount of light that gets captured by the receiving

16

fiber depends upon the distance of the transmission gap and the acceptance angle of the fiber, as well as the reflection at the right fiber end-face. Noting that the power is defined as

$$P = \int I(\rho, z) 2\pi\rho \, d\rho \qquad , \qquad (2.4)$$

one can define the attenuation or efficiency through the transmission gap as

$$\alpha = \frac{P_2}{P_1} = \frac{\int I(\rho, z) 2\pi\rho \, d\rho}{\int I(\rho, 0) 2\pi\rho \, d\rho} \qquad , \qquad (2.5)$$

which in turn can be simplified to as the following form:

$$\alpha = \frac{1 - e^{-2\left[\frac{w_0}{w(z)}\right]^2}}{1 - e^{-2}} \qquad . \qquad (2.6)$$

As the transmission gap distance z is altered by some desired measurand, the intensity of light transmitted into the receiving fiber is modulated and quantified by the detector. A sample plot of the attenuation versus the gap length is illustrated in Figure 2.2 for $w_0 = 4$ μm and $\lambda = 0.8$ μm. Since a sensor with linear sensitivity is desired, the working region for this sensor can be chosen as the linear region that spans from approximately 40 μm to 105 μm, where the slope is nearly constant.

This type of setup can be employed to measure several possible metrics depending on the mechanical configuration. By altering the mechanical arrangement, this setup can be used to measure vibration, force, temperature, or other physical quantities.
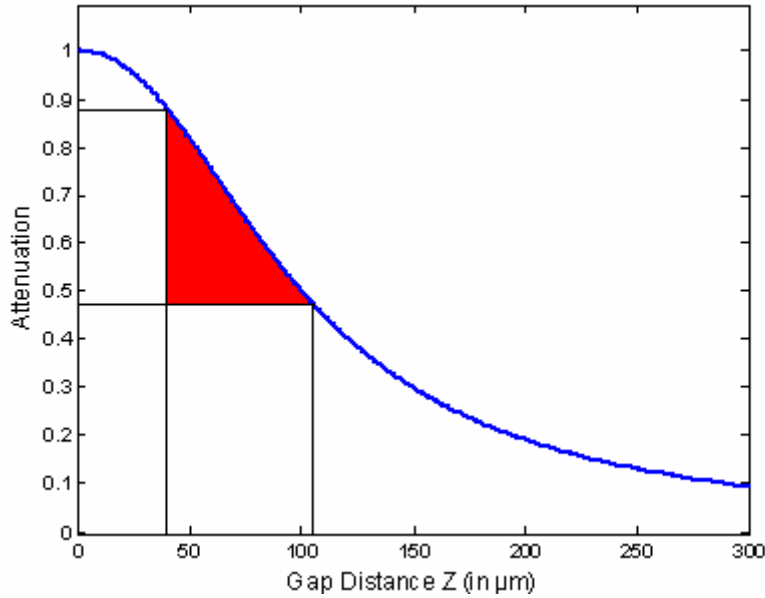
Figure 2.2: Sample plot of attenuation vs. transmission gap with the linear region highlighted.

Other configurations can be utilized to achieve different forms of transmission gaps to sense different metrics [25]. Some of the different types of transmission gap configurations are shown in Figure 2.3. For example, rather than having the fibers shifted axially to create a transmission gap (Figure 2.3(a)), they can be separated transversely with respect to each other (Figure 2.3(b)) or angled with respect to each other (Figure 2.3(c)). The output fiber can also be replaced by two fibers with a detector connected to each, where the transmitting fiber can move between the receiving fibers to create a differential (Figure 2.3(d)). In another possible group of configurations, the fibers are kept stationary and shutters such as optical wedges, moving lenses, or even gratings are employed in the transmission gap [25].
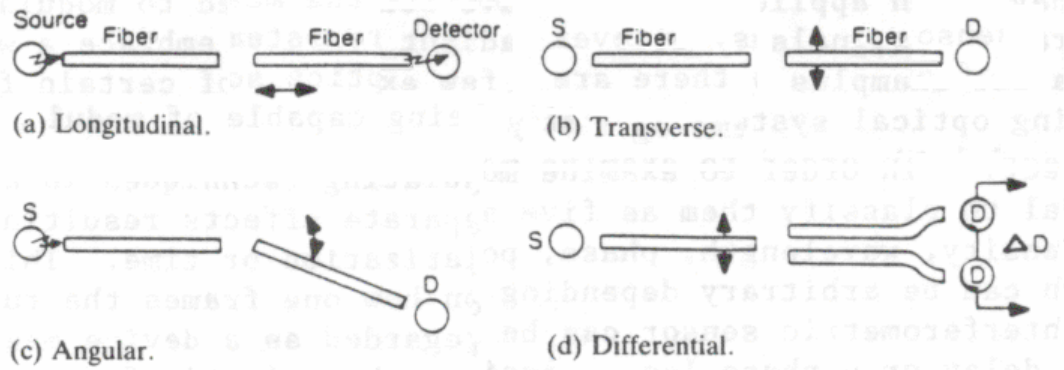
Figure 2.3: Examples of different transmission gap configurations [25].

In another useful transmission gap configuration, an external mirror that is subjected to the disturbance is used to reflect light into the receiving or output fiber. Generally, as shown in Figure 2.4, the configuration consists of a reflective surface replacing the fiber on the right side, while the output fiber is either relocated directly below the input fiber, or one optical fiber is utilized for both the input and output. In these cases, the mirror is generally utilized as a movable surface, and the transmission gap distance z is simply twice the distance between the fibers and the mirror.
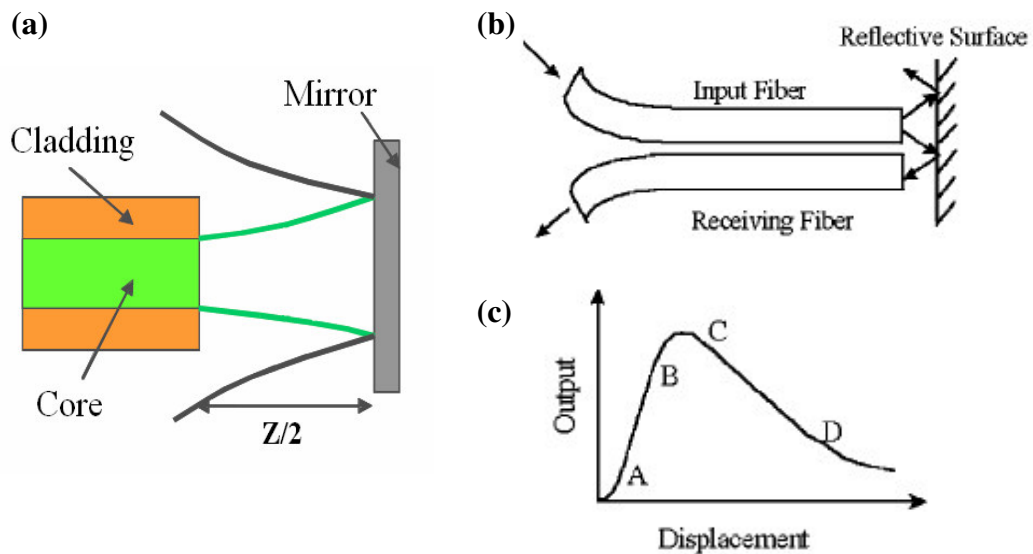
Figure 2.4: Transmission gap configurations utilizing a mirror [26,27].

The configuration of Figure 2.4(a) can be analyzed in a similar manner to that discussed in the configuration shown in Figure 2.1. The intensity output for the configuration shown in Figure 2.4(b) would take the form shown in Figure 2.4(c). In this graph, the first region with a positive slope corresponds to a transmission gap that is too short for the light to completely overlap the receiving fiber's core, and thus, as the mirror moves back, the receiving fiber captures more light until the core is fully enveloped. The configuration of Figure 2.4(b) actually has two possible working regions, which are the two nearly linear regions of the graph.

Since intensity is directly proportional to the measurand in all of the above discussed cases, it can be deduced that light sources with higher intensities will allow for a greater signal-to-noise ratio. Thus, when intensity based system configurations are used, it is desirable to use light sources with high power and optical fibers with large cores to ensure that the maximum intensity of light is generated and retained. In cases where a single mode operation is not needed, a multimode fiber is often used due to its significantly larger core diameter.

While high intensity light sources are always desirable, it is also important to consider the coherence property of the light source, which is often characterized by using coherence length. Coherence length is the distance over which a beam of light maintains a specific degree of coherence, where the photons of the light beam are in phase with each other. Based on the operation principles of an intensity based system, it is important to avoid any kind of interference in the working region; constructive and destructive interference would create sinusoidal fluctuations of intensity that would make it exceedingly difficult to determine a disturbance's

magnitude based solely on intensity values. In order to avoid this problem, low coherent light sources such as light emitting diodes and superluminescent diodes (SLDs) are often employed. They have short enough coherence lengths so that when they are operated in the working range of an intensity modulated system, the optical path difference is long enough to minimize interference. Since high intensities are still preferred for this type of system, an SLD is generally a good choice for a light source.

Based on the discussion made thus far, one can see that an intensity based sensor system is simple and straight-forward to use.   However, it is important to note that this simplicity can also be a major disadvantage. All of the previously discussed analyses do not take any intensity variations that are unrelated to the measurand into consideration. For example, if the light source's intensity output were to fluctuate, the sensing system would detect a change in intensity and correlate it to a disturbance to the measurand that never occurred. The same problem would arise if any variable losses occurred anywhere along the system. Thus, although it adds to the complexity and cost, sometimes it is necessary to add extra components such as a reference arm to be able to detect these potential fluctuations and take them into account.

2.1.2 Interferometry Based Fiber Optic Sensing System

An interferometry based sensor system, also frequently referred to as a phase modulated sensor system, is another commonly used sensor system. Rather than use some sort of intensity modulation, this system is designed to detect changes in the phase of the optical signal due to an applied disturbance. These phase changes are embedded in the interference. In order for the interference to occur it is usually

necessary to utilize a coherent light source. Interferometry based sensors have a high sensitivity and a high resolution, and thus, it is often utilized when high precision measurements are necessary. However, they are more complex than intensity based systems due to the need for a demodulator or a control system to maintain the required working region [25].

In an interferometry based sensor system, at least two different beams of light traverse different paths and then recombine, generating some type of interference which depends upon the optical path difference (*OPD*). The optical path difference is the difference in the optical path length that light beams travel before combining with each other, which is not only dependent on the gap distance, but also the refractive index of the medium that it travels through as well. This path difference will result in a phase change, which in turn is related to the disturbance. Similar to many other fiber optic systems, a mechanical component of some sort can be attached to the system to allow for a large variety of possible measurands. However, great care must be taken with the system as a whole since there are a multitude of effects that can affect the optical path difference traversed by a light beam.

In general, when two light waves with an optical path difference are combined, interference will occur. The electric fields corresponding to the two light beams can be expressed as

$$E_1(k,\phi_1) = A_1 \exp\left[w(k)t + j\phi_1\right] \tag{2.7}$$

$$E_2(k,\phi_2) = A_2 \exp\left[w(k)t + j\phi_2\right] , \tag{2.8}$$

where A_i is the ith wave amplitude, k is the wave number defined as $k=2\pi/\lambda$, and ϕ_i is the optical phase of the ith field. When the two beams are combined, the resulting intensity can be determined as

$$I(k) = \langle E_1 + E_2 \rangle \langle E_1 + E_2 \rangle^* \quad , \tag{2.9}$$

where the * represents the complex conjugate and <> represents an ensemble average. The intensity of interference can then be expressed in the form

$$I = I_1 + I_2 + 2\sqrt{I_1 I_2}\, \gamma(k, OPD)\cos\Delta\phi \quad , \tag{2.10}$$

where I_1 and I_2 are the intensities of the two light beams, $\Delta\phi$ is the difference in phase, γ is the visibility function, and OPD is the optical path difference of the two beams. The visibility function is defined as:

$$\gamma = \exp\left[-\left(\frac{OPD}{l_c}\right)^2\right] \quad , \tag{2.11}$$

where l_c is the coherence length of the light source (the maximum achievable visibility value is 1). The coherence length, an inherent property of a light source, is a function of the wavelength λ and the spectrum width $\Delta\lambda$ of the source, as shown below

$$l_c = \frac{\lambda^2}{\Delta\lambda} \quad . \tag{2.12}$$

Subsequently, the visibility of the interference can be determined as

$$V = \frac{2\sqrt{I_1 I_2}}{I_1 + I_2}\gamma \quad . \tag{2.13}$$

The better the visibility, the higher the amplitudes of the interference fringe will be. From Equations (2.11) and (2.13), it can be seen that the OPD is critical in

23

determining the visibility of the interference. Thus, in order for an interferometer to function properly with high visibility, it is generally necessary for the *OPD* to be much shorter than the coherence length of the light source. If this condition is met, the general output of a two beam interferometer can be simplified to the form

$$I = I_1 + I_2 + 2\sqrt{I_1 I_2} \cos \Delta\phi \quad . \tag{2.14}$$

In this case, a coherence light source such as a laser is usually used and the system is called a conventional fiber optic interferometry system. Based on Equation (2.14), a typical output of a conventional fiber optic interferometry system is plotted in Figure 2.5. As shown in this figure, the sensor has a maximum sensitivity at the points where $\Delta\phi = (2n-1)/\pi$ (*n* is an integer). These points of maximum sensitivity are known as quadrature points. However, the peaks and valleys of the sine curve show very little sensitivity, as a change in phase difference hardly affects the intensity of interference. Thus, the operations of sensors in these regions should be avoided if possible. In fact, these sensors are typically operated within a "linear" range in the vicinity of a quadrature point, and hence, they have limited dynamic range (< ¼ wavelength). In addition, the sensor operating point may suffer from drift due to environmental perturbations and light source wavelength fluctuations. In practice, in order for an interferometer to have a high sensitivity and function properly, highly coherent and stable light sources with a low noise are necessary. In many cases, one needs to compensate for the shifts of the operation point and the wavelength fluctuations in a laser light source by applying a control scheme. However, schemes used for stabilization of such sensor systems increase the system complexity [28,29].
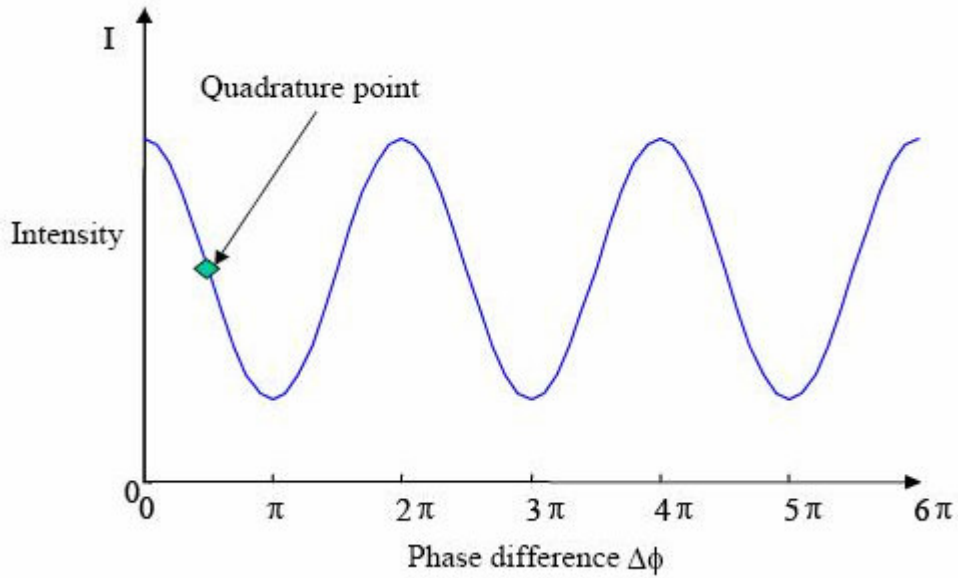
Figure 2.5: Intensity variation with respect to the optical phase difference [30].

There exists another approach of interferometry that makes it possible to reduce the drawbacks commonly seen in conventional interferometry based sensor systems. This approach makes use of what is called low coherence or white light interferometry, which allows for a much larger dynamic range with high resolution, negates 2π periodic ambiguity, and provides immunity to light source intensity and wavelength fluctuations [31,32].

Low coherence interferometry utilizes a low coherence, broadband light source, such as LEDs, SLDs, or halogen lamps. Similar to conventional interferometers, the optical path difference of light waves can be modulated by the measured parameter and determined through an interference pattern analysis. However, unlike the conventional interferometry based sensor system, a low coherence system can be processed either in the phase domain or in the spectrum domain. In phase domain processing, a differential optical phase between a sensing

25

interferometer and a reference interferometer is measured. The optical path difference of the reference interferometer is chosen to match that of the sensing interferometer. Owing to the differentiation of the phase signal between the two interferometers, this technique has immunity to wavelength and power fluctuation induced noise, permits a short effective sensing cavity, and yields a high resolution, and a large dynamic range [28]. When a spectral domain processing technique is used, a spectrum analyzer is often utilized as the optical processing element. Due to the interference, the intensity will have periodic cosine fringes throughout the entire spectrum span of the light source. The spacing between two adjacent fringes depends on the wavelength of the source and the optical path difference of the sensor. A representative spectrum domain output of a low coherence interferometer is shown in Figure 2.6. As the wavelength or *OPD* is changed, the location and spacing of the interference fringes are altered. Thus, in a low coherence system, by analyzing the change in interference fringes of the spectrum, one can obtain the change in the *OPD* and in turn determine the magnitude of the disturbance.
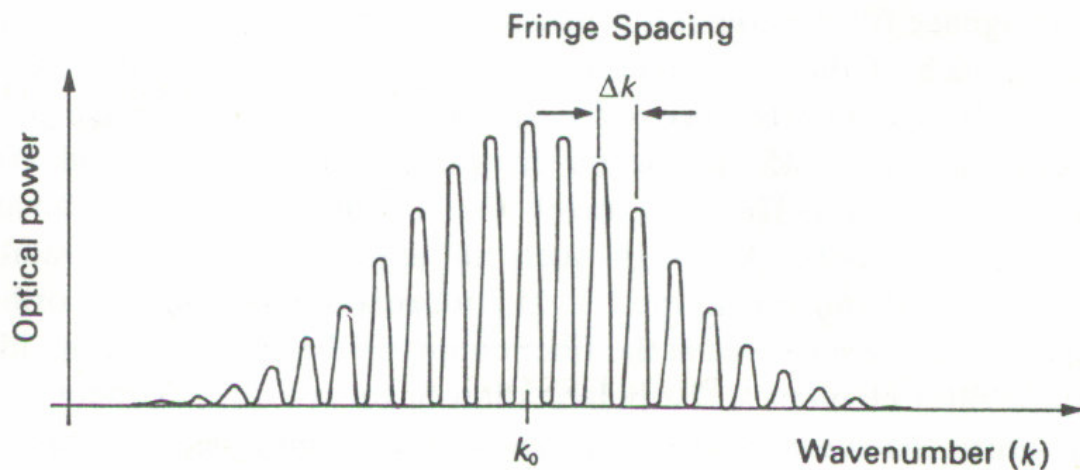
Figure 2.6: Spectral fringes of a low coherence fiber optic system recorded from a spectrometer [31].

2.2 Optical System Design

2.2.1 Intensity Based System Configuration

In the first sensor system developed for the rodent tail pressure measurements, an intensity based system configuration was used, where pressure changes were measured as a change in light intensity. As shown in Figure 2.7, the designed system consists of a 1300 nm SLD light source, a 1×2 3 dB coupler, a digital power meter, and a fiber optic pressure sensing element. The SLD source is utilized to obtain enough intensity while still maintaining low coherence. Single mode fiber (SMF), one of the most commonly utilized optical fibers, is used to maintain a single mode light beam. The power meter is designated to get a power reading in the 1300 nm range.
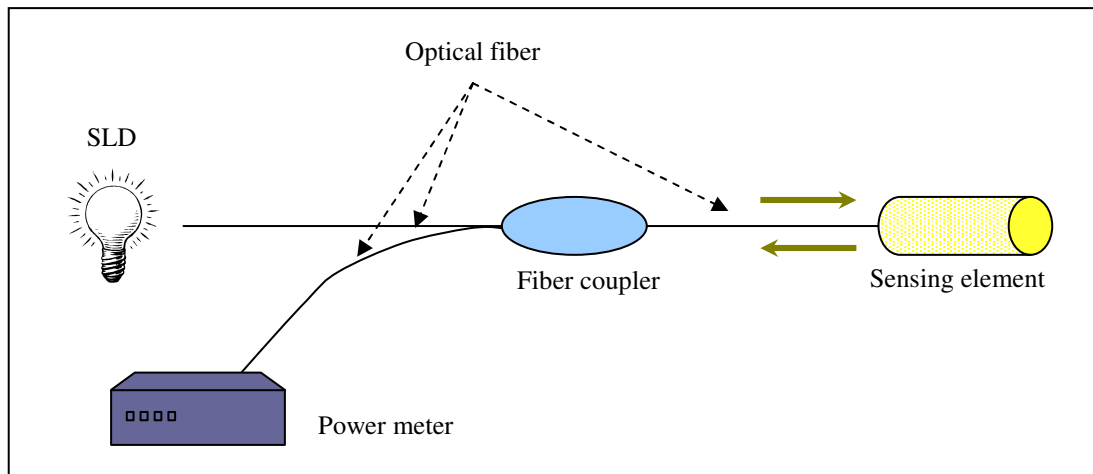
Figure 2.7: Schematic of an intensity based system configuration designed for rodent tail pressure measurements.

Low coherent light, which is generated by the SLD source, is coupled to an optical fiber and travels through the 3 dB coupler with a 50:50 splitting ratio into another optical fiber leading to the sensor. For this intensity based system, the sensing element must be able to modulate the light intensity depending on the pressure applied. In this case, one approach, which is equivalent to the transmission gap configuration described in Figure 2.4(b), is to utilize a sensor that has a cleaved fiber end perpendicular to a movable mirror as the pressure sensing element. When pressure is applied, the mirror moves closer to the fiber end so that the light intensity returned back into the fiber is increased. The returned light traveling through the coupler is received by the power meter, where the light intensity can be integrated over the fiber cross-section area to determine the power of the returned light beam. The power reading from the power meter is significantly lower than the power emitted by the SLD due to various losses throughout the system including the splitting due to the coupler, coupling losses, fiber attenuation, transmission gap loss, and an imperfect reflection of the mirror. While minimizing the loss is desirable, the aforementioned losses can all be determined as fairly constant quantities. Hence, the intensity change obtained from the power meter depends on the light returned from the sensing element, and an increase in pressure can be associated with an increase in the power reading.

It should be noted that minimizing the loss is very important for this system configuration since the performance of the sensor system depends largely on the received light intensity level; the fewer the losses the greater the light intensity that reaches the power meter. Thus, minimizing the loss can help realize a sensing system

with a high signal-to-noise ratio and a high resolution. As previously mentioned, a major drawback of this design is its sensitivity to power fluctuations; this design only relies on the stability of the SLD source and does not compensate for potential fluctuations.

2.2.2 Low Coherence System Configuration

A low coherence interferometer based optical sensing system has also been developed through this thesis work for rodent tail pressure measurements. As shown in Figure 2.8, this system includes a broadband light source, a 1×2 3 dB coupler, a Fabry-Perot interferometric sensing element, and a high-speed spectrometer. In this case, the light beam generated from the broadband source is guided by a fiber through the coupler to the Fabry-Perot sensing element. A Fabry-Perot configuration uses two mirrors (a partial mirror and a second mirror, which can be either a partial or a complete mirror) to form a cavity. A pressure induced movement of one of the mirrors results in a change of the *OPD* of the low coherence system, which changes the interference fringes of the spectrum, as discussed previously. Details on the design and fabrication of the Fabry-Perot sensing element are described in Chapter 3. The reflected light from the Fabry-Perot sensor is then coupled back to the spectrometer through the coupler. Specialized software that will be discussed later in this section allows for acquisition of the spectrum data. This data is then used to obtain the change in the cavity length of the sensing element through the detection of the change in the interference pattern.
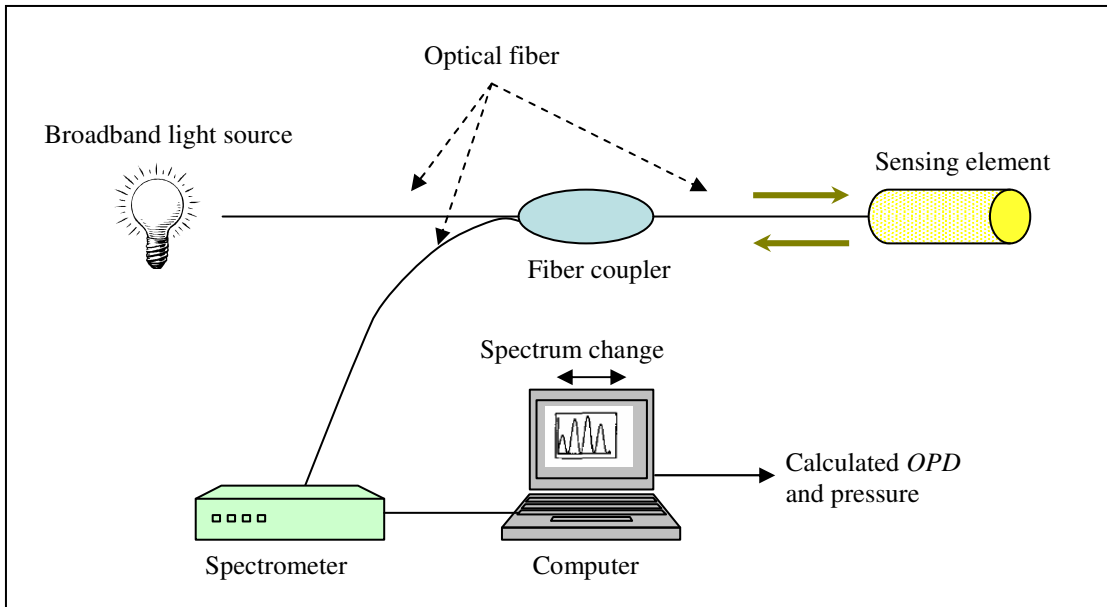
Figure 2.8: Schematic of a low coherence interferometry based sensor system designed for rodent tail pressure measurements.

The spectrometer utilized was a miniature fiber optic spectrometer (USB4000 from Ocean Optics) with an integration time as low as 10 µs and a configurable detector range between 200 nm and 1100 nm. The integration time can be considered to be the same as the shutter speed of a camera. A longer time will allow for more light to enter and thus will result in a reflected spectrum having higher intensities, but the rate of sampling will suffer. The intensity of returned light depends primarily upon the power of the light source, reflectivity of the mirrors in the sensing element, and the user-specified integration time of the spectrometer. However, since the data processing of the returned spectrum relies solely on the wavelengths of the peaks, a high intensity of returned light is not a primary goal. While a high intensity will allow for less noise in the system, it has a direct inverse relationship with respect to the integration time, and subsequently, the sampling rate. If the returned light has

sufficient intensity so that one can clearly distinguish the individual peaks of the reflected spectrum, the intensity of light can be sacrificed for a higher sampling rate. Thus, the frequency is primarily dependent on the power of the light source and the reflectivity of the sensing element's mirrors; high powered light sources and high reflectivity mirrors will allow for shorter integration times and higher sampling rates.

A Tungsten Halogen Light Source (HL-2000 from Ocean Optics) with an output of 20 W was employed due to its high power and low coherence properties. For the system configuration shown in Figure 2.8, only a small percentage of the initial light will return to the spectrometer due to the coupling ratio, various losses throughout the system, and the reflection efficiency of the sensing element. Due to the low percentage of returning light as well as the dependence of frequency on light intensity, a high powered light source is necessary for achieving optimum performance. The power output spectrum for the HL-2000 can be seen in Figure 2.9(a). Based on the light source properties, a higher operating wavelength range is desired for maximizing light intensity.

To maintain an ideal balance between the resolution and the light detection efficiency, the spectrometer has been configured with a specific grating (Grating #6). The efficiency curve and operating range for the grating are illustrated in Figure 2.9(b). Since a higher intensity of light is desired, gratings with good efficiencies at higher wavelengths are required. Of the several gratings that meet this criterion, Grating #6 had the shortest spectral range of approximately 300 nm, allowing for the highest resolution and making it the ideal choice. An operating range of approximately 700 nm to 1000 nm was chosen to maximize the grating efficiency and

31

the light source output. Due to the chosen operating range, a 780 nm single mode optical fiber and an 830 nm coupler were used to maintain the single mode condition.

The spectrometer was also configured with a bandwidth filter grating and an entrance slit of 10 µm for higher resolution and increased light detection. The corresponding resolution of the spectrometer is approximately 0.5 nm at the full width at half maximum (FWHM).

(a)   (b)
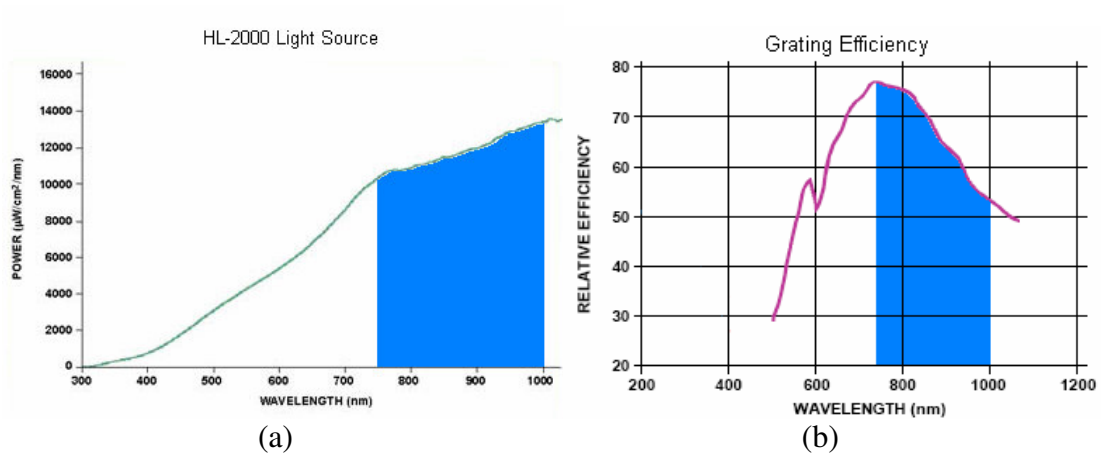
Figure 2.9: (a) Output power spectrum of HL-2000 [33] and (b) reflective efficiency of Grating #6 [34], where the selected system operating range is highlighted.

Along with the spectrometer, specialized software provided by Ocean Optics called SpectraSuite Spectroscopy Platform Software was used. This software has the capability to complete an iteration of integration and data transfer within 10 ms. By using this software, one is able to record data for a single spectrum as well as a continuous stream of spectrum readings for a specified length of time using the high speed acquisition function. This feature allows for the system to be capable of not only making static pressure measurements, but also dynamic pressure measurements.

Chapter 3: Miniature Fiber Optic Pressure Sensor Development

In this chapter, the following types of miniature pressure sensors are developed: i) a solid-tip sensor that is used in the intensity based sensor systems and ii) a diaphragm based Fabry-Perot sensor that is used in the low coherence interferometer sensor system.

3.1 Solid-Tip Sensors

3.1.1 Concept of the Solid-Tip Sensor

As mentioned in the previous section, the proposed intensity based system requires a pressure sensing element that will modulate the returned light intensity depending upon the pressure applied. The sensor developed for the intensity based system configuration utilizes a deformable polymer tip attached to the cleaved end-face of an optical fiber and a glass capillary tube. The pressure sensing tip is coated with a thin layer of titanium, acting as a movable mirror. Applied pressures cause the polymer sensor end to deform and the mirror to move closer to the fiber end. A schematic of the solid-tip sensor is shown in Figure 3.1.
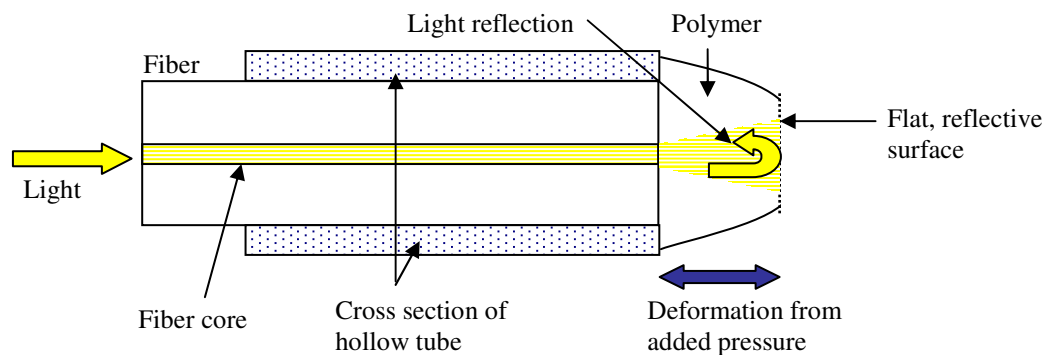
Figure 3.1: Schematic of the solid-tip sensor.

The sensor uses a SMF inserted into an approximate 1 inch length of a glass capillary tube. There are varying sizes of capillary tubes available. For feasibility and testing purposes while still maintaining size constraints for the rat tail, a capillary tube with an outer diameter of 363 µm is utilized. The tube has an inner diameter of 150 µm, while the diameter of a stripped fiber is 125 µm. This allows for some clearance so that the fiber can be easily inserted into the tube without excessive friction. The pressure sensing element utilizes a solid bubble of a flexible, photosensitive polymer as a deformable sensing tip. The deformable polymer bubble functions as a propagation medium separating the fiber end from the mirror. A detailed fabrication procedure is provided in Section 3.1.2.

Light travels through the optical fiber until it reaches the fiber end-face. The transmitted light then propagates through the polymer until it reaches the mirror, where the light is reflected and travels back into the fiber core. Due to diffraction of the light beam, it expands when it travels through the polymer. Thus, the propagation distance (the distance between the fiber end and the mirror) directly affects the intensity of light returned to the fiber core. Under an applied pressure, the polymer bubble deforms and the propagation distance decreases, subsequently increasing the light intensity returned to the fiber. The greater the applied pressure, the greater the deformation of the sensor tip and the higher the intensity of returned light. As mentioned in the previous chapter, for the intensity based system configuration, the returned light from the sensor travels through the fiber to a power meter, where the light intensity is integrated and the optical power is determined.

The expected performance of the sensor can be determined by utilizing Equations (2.1)-(2.6). Since the propagation medium is a polymer material rather than air, it is necessary to adjust the equation with a different refractive index. Although the exact refractive index of the polymer is unknown, it can be estimated as approximately 1.4 for analytical purposes, a common value for other cured polymers adhesives. The SMF core radius of 4.5 µm is used for the beam waist w_0 and the center wavelength is chosen as 1.3 µm. By using these values, the sensor's performance can be predicted, as shown in Figure 3.2. Based on this figure, an approximate linear region can be observed when the propagation distance is between 20 µm and 60 µm. Since this sensor will only be used to measure increases in pressure (i.e., the transmission gap will only decrease in length), the initial propagation distance was chosen to be 60 µm.
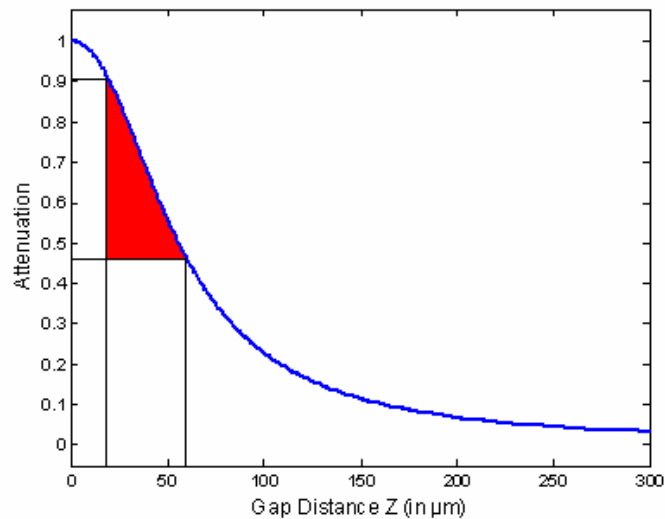
Figure 3.2: Intensity attenuation with respect to polymer gap distance for the solid-tip sensor, with a linear region between 20 µm and 60µm.

3.1.2 Sensor Fabrication

The fabrication of this solid-tip sensor requires the following materials: SMF-28 optical fiber from Corning, TSP150375 capillary tubing (150 µm I.D., 363 µm O.D.) from Polymicro Technologies, NEA123 flexible optical adhesive from Norland Products, and room temperature curing epoxy.

The fabrication steps are as follows.

i. *Cleave a glass capillary tube and a SMF.* Approximately one inch of glass capillary tube is cut and properly cleaved to achieve an end-face perpendicular to the tube axis. The tube has a 150 µm inner diameter, 363 µm outer diameter, and 20 µm thick polyimide coating for abrasion resistance and structural strength. The SMF is cleaved on both ends. One end of this fiber is used to receive the light returned from the pressure sensing element while the other end is connected to a coupler according to the system configuration.

ii. *Attach a polymer tip to the end of the fiber and the tube*. The prepared fiber end is inserted into the capillary tube until it is nearly flush with the tube end. Note that the fiber end is not fixed in any way and can still be adjusted when necessary. A drop of the NEA123 photosensitive polymer is placed on a flat surface such as a microscope slide. By using a one-directional translation stage, the end of the tube is advanced toward the drop of the gel-like polymer until the end surface just touches the polymer. The polymer inevitably gets siphoned into the tube, which is a beneficial after-effect since it fills the empty space between the tube and fiber end as well as surrounds the fiber, helping to keep it in place after curing is complete. With the tube end still flush against

the surface of the polymer drop, the fiber is adjusted to allow for more siphoning and shape manipulation of the polymer bubble at the tube end. As the tube is retracted from the polymer drop, a semi-ellipsoid of polymer will remain on the tube end.

iii.   *Adjust the thickness of the polymer layer*. The desired thickness of the polymer bubble is approximately 60 µm for this sensor, as discussed previously in Section 3.1.1. By adjusting the insertion depth of the fiber and re-dipping the tube end, the cavity length and shape of the end bubble is manipulated and monitored using a stereo microscope with a magnification of 80 times. Photographs taken with a digital microscope camera in conjunction with the measurement software is used to estimate the distance of the fiber end and the thickness of the polymer bubble.

iv.   *Cure the polymer tip under ultraviolet (UV) light*. When the desired thickness is achieved, an UV lamp is used to cure the polymer. Since greater elasticity helps the sensor achieve a higher sensitivity, the polymer tip is cured until it is just completely solidified. For the size of the sensor tip and conditions in this research, the cure time was found to be approximately 5 minutes to solidify the polymer. Due to the aforementioned siphoning of the polymer, curing the polymer not only solidifies the sensor tip, but also helps to fix the fiber in place. Thus, theoretically the only way to change the cavity length and subsequently the intensity would be to apply a pressure onto the sensor tip to deform the polymer.

v.   *Immobilize the fiber inside the capillary tube*. Room temperature cured epoxy is coated on the non-sensing end of the capillary tube and along the protruding fiber to further fix the fiber in place. An appropriate amount of epoxy is used to additionally strengthen the most fragile area of the sensor: the gap of the bare fiber extending from the capillary tube end to the fiber coating. Thus, the epoxy not only helps to make the sensor more durable, but also ensures the fiber is truly fixed and immobile inside the capillary tube.

vi. *Polish the polymer tip to obtain a smooth, flat surface*. A movable mirror is an integral part of the sensor in order for the system to function. In order to create a mirror parallel to the fiber end, the polymer tip must be flattened and smoothened. The very end surface of the polymer tip is polished by using a standard fiber polishing machine. When this step is completed, the end of the polymer tip has a flat and polished surface.

vii. *Create a mirror on the polished surface*. In order to create the mirror, a layer of reflective metal is sputtered onto the end surface by using a DC Magnetron Sputtering machine. Sputtering is a process whereby a thin film of a chosen material (target) is deposited onto a desired surface (substrate). By first creating a vacuum and then producing gaseous plasma with Argon gas, the plasma ions are then accelerated into the chosen target. When hit by these ions, the target is eroded and neutral particles of the target's source material are ejected in a straight line until they hit the substrate. Thus, when the sensor ends are placed in the path of the particles by a custom-made holder, a thin layer of reflective metal is deposited onto their end surfaces to create an

effective mirror. Photographs of the sputtering machine's chamber and the specially made holder are shown in Figure 3.3 and Figure 3.4.
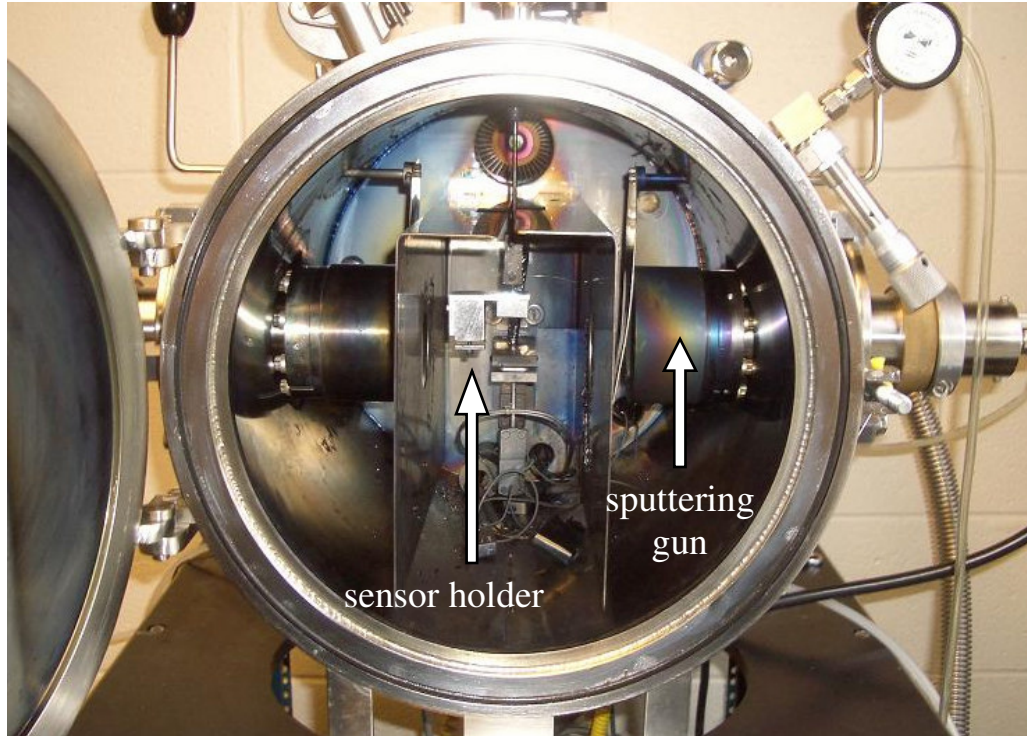
Figure 3.3: Inside view of the DC Magnetron Sputtering machine.
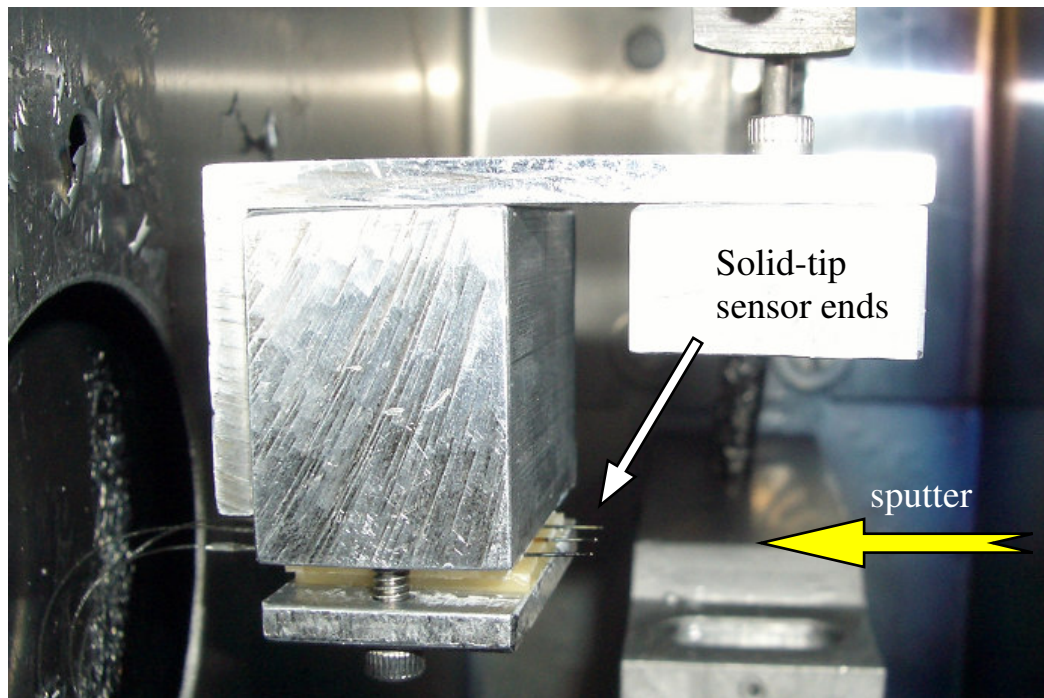
Figure 3.4: Specially fabricated sensor holder for sputtering.

A titanium target is used for this sensor to create the reflective end surface. The thickness of the sputtered film is a function of the target material, distance from the gun to the substrate, pressure conditions in the chamber, and sputtering time. With constant pressure conditions and sputtering distance, the experimental results suggested that a sputtering time of approximately 20 minutes is adequate to create a thin titanium film of 1 μm thickness with good reflective properties.

viii. *Create a connector on the free end of the optical fiber.* This is the last step to complete the sensor, in which the standard process for making an FC connector is used.

A brief summary of the fabrication process is illustrated in Figure 3.5, and an image of a completed solid-tip sensor is shown in Figure 3.6.
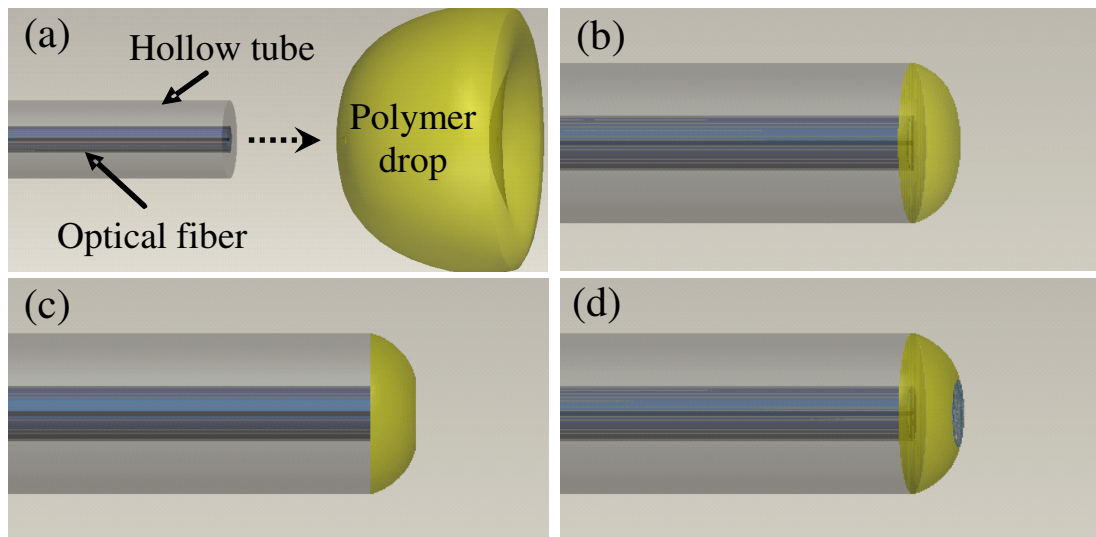
Figure 3.5: Schematic of the fabrication steps: (a) dipping of tube and fiber into polymer, (b) adjusting of fiber and UV curing of polymer bubble, (c) polishing of end-face, and (d) sputtering of reflective layer.

360μm
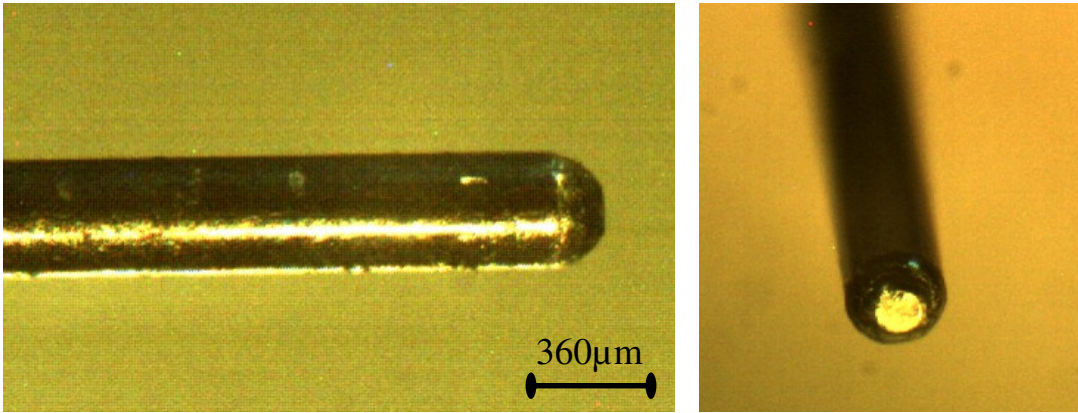
Figure 3.6: Photographs of a completed solid-tip pressure sensor; image captured by using a digital camera and a stereo microscope with 40× magnification.

3.1.3 Summary of the Solid-Tip Sensor Design

There are several advantages innate to this sensor design compared to other similar intensity based sensors. The fact that the propagation medium between the fiber and the mirror is a solid polymer eliminates the possibility of dust and debris getting inside the cavity during fabrication. Particles present inside the propagation medium can cause blocking of light, dropping the reflected intensity or even rendering the sensor useless. The solid sensing tip is also a very durable design as compared to many other designs, such as a thin diaphragm design. A solid polymer tip in theory should be able to withstand higher pressures and harsher environments without damage to the sensor itself. This is essential to allow for repeated use of the same sensor inside the rat tails.

However, there are limitations associated with the design and fabrication of the solid-tip sensors. Some drawbacks of this design concept include that it is expected to be less sensitive than other design types. Due to the entire solid-tip

material that must be deformed under the applied pressure, the response of the sensor is expected to be less than that of a thin diaphragm. In addition, this fabrication technique makes it impossible to test if the sensor is functional until it is completely fabricated; only after the entire process is complete can the sensor be tested to see if it is sensitive to any pressure changes. Furthermore, this design and fabrication procedure only allows for one sensor to be produced at a time. Due to the inherent difficulties in certain steps of the fabrication process, a higher deviation of sensor characteristics would be anticipated in these procedures than a sensor design that allows for batch fabrication.

The notable difficulties in the fabrication procedures are as follows. First, the size and shape manipulation of the polymer bubble at the sensor end is quite difficult due to inconsistencies in the volume of polymer siphoned into the tube, as well as the fact that the fiber end can be moved. Mastering this step takes quite a bit of practice, and even then it is nearly impossible to achieve the exact thickness of polymer desired. However, due to the relatively large working range of an intensity based system, deviation from the desired polymer thickness will still allow for a functional sensor simply with slight changes in properties such as maximum output intensity. Furthermore, it is very tricky to properly polish the end of the polymer when creating a flat surface. Care must be taken so that an excessive amount of polymer is not polished off, leaving a very small polymer thickness. Controlling the depth of which the polymer is flattened is hardly consistent, and even then the surface is not guaranteed to be completely smooth. Smoothness of the surface is obviously desired

to allow for the light to effectively reflect off the mirror. Again, mastering this step requires much practice.

3.2 Diaphragm Based Fabry-Perot Sensors

3.2.1 Concept of the Fabry-Perot Sensor

For the low coherence system configuration discussed in Chapter 2, the type of interferometric sensor utilized is a Fabry-Perot interferometer (FPI). In brief, as opposed to a two-beam interferometer where only two beams of light are combined to create interference, a FPI is generally a multi-beam interferometer in which light is divided into many separate paths before mixing. The FPI is one of the most common multi-beam interferometers, which contains an optical cavity formed between two mirrors. Due to the partial reflections of the mirrors, the input light is traversed many times. A schematic of a typical Fabry-Perot interferometer is shown in Figure 3.7. For a Fabry-Perot cavity of a certain length L, light that enters the cavity will be reflected and transmitted by the two mirrors in such a way that the phase delay for a round trip is dependent on twice of the cavity length. A disturbance in the cavity length will cause a change in the phase delay for the light on every pass through the cavity, causing a larger change in interference than a two beam interferometer could achieve. Additionally, due to the partial reflections, each successive light beam will have reduced amplitude dependent upon the reflectivity of the mirrors. Thus, depending on the reflectivity of the mirrors, there can be a varying number of reflections that occur before the beam intensity becomes negligible. In a case where mirrors of weak reflectivity are utilized, the attenuation of the light intensity from one

pass can be so great that all other passes become insignificant and a two-beam interferometer assumption can be made.
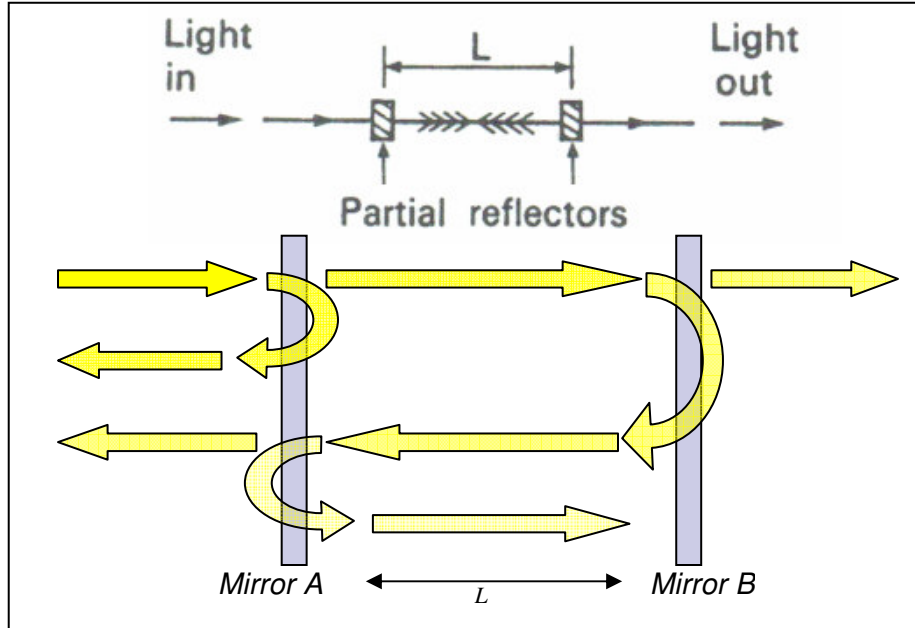
Figure 3.7: Schematic of a typical Fabry-Perot interferometer [31].

In this work, the design of the Fabry-Perot sensor utilizes a fiber end as a partial mirror, and a reflective diaphragm tip enclosing an air cavity as another mirror. The sensor uses a 780 nm single mode fiber inserted partially into a section of glass capillary tube. A diaphragm created at the end of the hollow tube acts as a pressure transducer. The diaphragm is made from a layered combination of photosensitive polymer and reflective nickel-titanium. Here, nickel-titanium is used rather than titanium because previous trials revealed it had a smoother surface. The schematic of the Fabry-Perot pressure sensor is shown in Figure 3.8.

As seen in Figure 3.8, light travels through the optical fiber until it reaches the fiber end-face. For a well-cleaved fiber end-face without the reflective coating, there is an approximate 4% reflection at the fiber end. The transmitted light propagating through the air cavity is reflected by the diaphragm back to the fiber. Thus, the optical path difference of a reflected light beam is twice that of the cavity length. The combination of the reflected light beams causes interference, which is then detected by the spectrometer. Due to the low reflectivity of the partial mirror, this Fabry-Perot sensor can be approximated as a two-beam interferometer. An applied pressure to the sensor causes the diaphragm to deform and the cavity length to shorten; this alters the interference spectrum so that there is a shift in the locations and spacing of the fringe peaks. The cavity length change can thus be obtained by using an interference equation, which can be further related to the corresponding pressure values through calibration experiments.
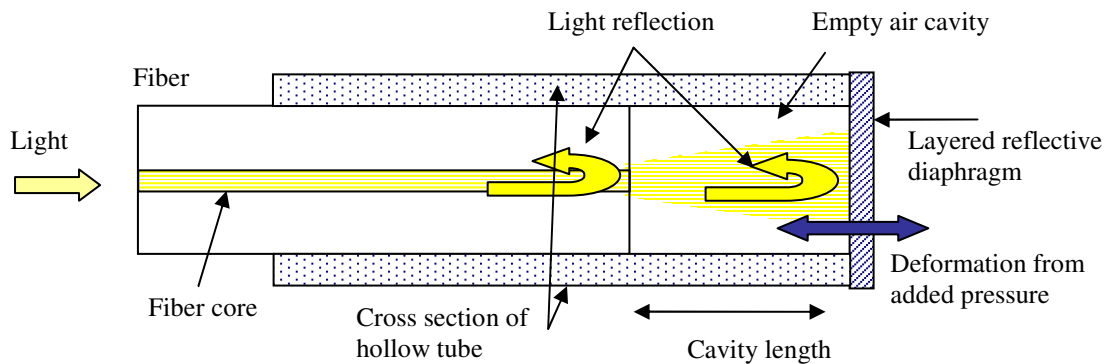
Figure 3.8: Schematic of the designed Fabry-Perot pressure sensor.

The sensor's mechanical component, the diaphragm, can be modeled as an edge-clamped circular plate. An analytical solution of this model is well known.

Based on this model, the diaphragm deflection as a function of the applied pressure can be written as [35,36]:

$$\Delta L = \frac{3(1-v^2)(a^2-r^2)^2}{16Ed^3}\Delta P \qquad , \qquad (3.1)$$

where v and E are the Poisson's ratio and Young's modulus of the diaphragm material respectively, a is the diaphragm radius, d is the thickness, r is the radial distance from the diaphragm center, and ΔP is the applied pressure change. Based on this equation, the deflection varies from zero at the clamped edge to the maximum value at the center of the diaphragm. Since the fiber is aligned with the center of the diaphragm, only the maximum deformation at the center is considered; that is, $r = 0$ in Equation (3.1), leading to

$$\Delta L = \frac{3(1-v^2)a^4}{16Ed^3}\Delta P \quad . \qquad (3.2)$$

In Figure 3.9, a chart of expected center deflection with respect to the pressure change for diaphragms with different thicknesses is presented. As expected, the deformation is linearly proportional to the pressure change. The diaphragm center deflections can vary drastically with respect to small differences in the diaphragm thickness. However, it is important to note that a simplified model has been used here. In this model, the diaphragm is considered to be uniform and constructed of one single material. For this analysis, the estimated values for the Poisson's ratio and the Young's modulus of nickel-titanium were utilized as the values for the diaphragm material.
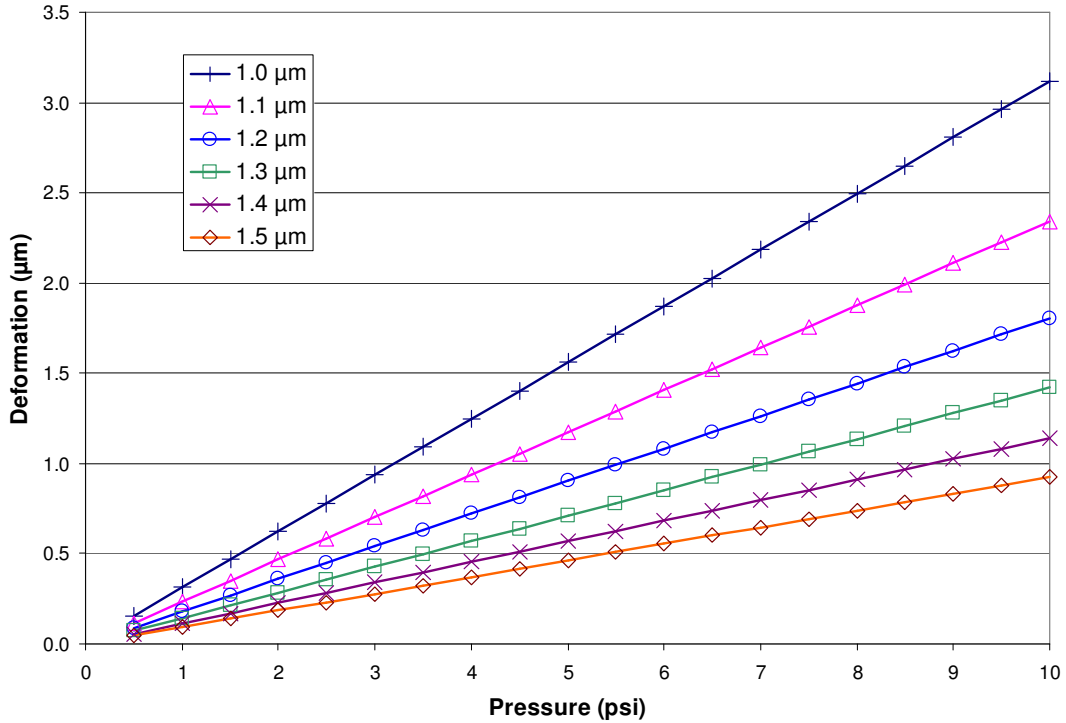
Figure 3.9: Predicted deformations of diaphragms of differing thicknesses.

Although there are a variety of sensing methods and configurations that can be utilized for a Fabry-Perot sensor, the optical system chosen here is a low coherence interferometry system with spectrum domain signal processing. This system allows for good sensitivity while still maintaining a rather large dynamic range. The system detects the interference fringes in the spectrum domain to obtain the cavity length of the Fabry-Perot sensor, which corresponds to the deformation of the diaphragm caused by an applied pressure. The high speed spectrometer can be used to obtain the interference pattern in the spectral domain. Two representative interference patterns are shown in Figure 3.10. Based on the interference pattern, the cavity length L of the Fabry-Perot sensor at any given time can be obtained as [12]:

$$L = \frac{\lambda_1 \lambda_2}{2(\lambda_2 - \lambda_1)} \qquad , \qquad (3.3)$$

where λ_1 and λ_2 are any two adjacent reflectance peaks. The sensor system is robust to the power fluctuations of the light source and various bending and environmental disturbance induced intensity drifts due to the fact that such fluctuations and drifts do not change the peak wavelengths of the interference fringes.

Depending on the sensor's cavity length, there can be a varying number of visible peaks within the spectral range of the interference pattern. Since determining the cavity length only requires two adjacent peaks, it is possible to perform several calculations from one reflected spectrum to obtain averaged cavity length values at any given time. To avoid errors, the first peak on the spectrum is discarded, as well as any peaks after a certain wavelength in which the peaks begin to lose visibility and accuracy. The remaining peaks are all used to generate several cavity length values, from which the average and standard deviation are determined. The average value is taken to compensate for any erroneous peaks, while the standard deviation is taken to judge the precision of the individual cavity length value. A high standard deviation implies poor visibility of the spectrum with difficulties isolating the individual interference peaks; this causes the accuracy of the calculated average cavity length to suffer. Since the standard deviation will vary greatly with different cavity sizes (i.e. different sensors), it is divided by the average cavity length to obtain a dimensionless percentage. Figure 3.10 shows two different spectra at different cavity lengths, where the peaks used for cavity length calculations in Equation (3.3) are denoted by a circle or a diamond. As the diaphragm deflects and the cavity length is reduced, the interference fringes shift to the left and the gaps between the peaks gradually

increase. In Figure 3.11, two different spectra from the same sensor are compared. One of the spectra has good visibility and the other has poor visibility. The spectrum with good visibility has a standard deviation percentage of 1.23%, while the other is 19.10%.
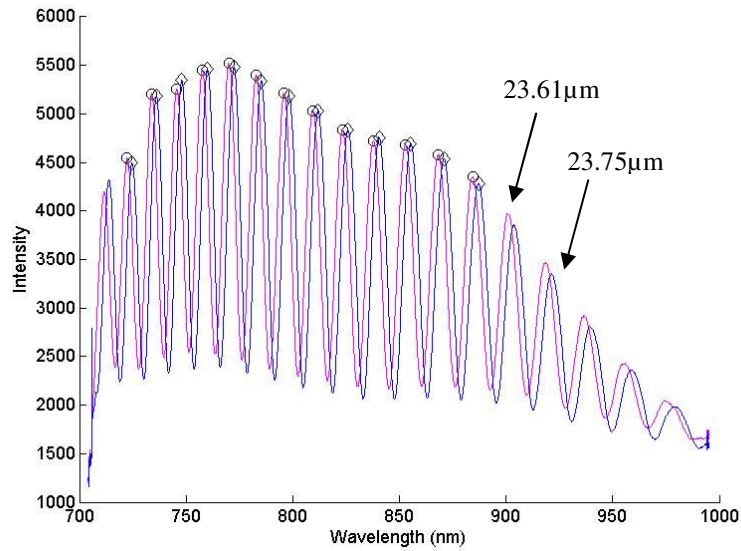

Figure 3.10: Interference patterns at two different Fabry-Perot cavity lengths.
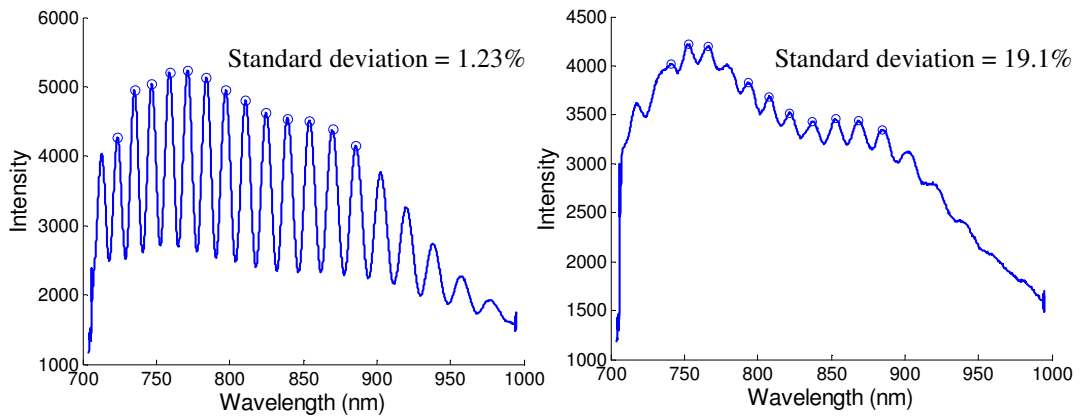
Figure 3.11: Good and poor visibility interference patterns.

49

3.2.2 Sensor Fabrication

The fabrication of this Fabry-Perot sensor requires the following materials: 780 nm single mode optical fiber from Fibercore, TSP150375 capillary tubing from Polymicro Technologies, NOA68 flexible optical adhesive from Norland Products, and room temperature curing epoxy. This optical fiber allows for the light to maintain single mode at lower wavelengths than the conventional SMF-28 fiber by having an altered numerical aperture and smaller fiber core. The fabrication procedures for this sensor allow for multiple sensors to be constructed simultaneously. Thus, a batch of sensors can be obtained with very similar properties.

The fabrication steps for the Fabry-Perot pressure sensor are as follows.

i. *Cleave the fibers and the glass capillary tubes.* Approximate one inch sections of the capillary tube are properly cleaved with the same method as described in the solid-tip sensor fabrication. Appropriate lengths of optical fiber are also cleaved with a standard cleaver, leaving more than one inch of stripped length for the sensing end.

ii. *Create and pre-cure polymer thin film.* A conventional Petri dish is partially filled with distilled water. A small wire lasso is placed in the water for later use. Care must be taken so that no part of the lasso (other than the handle) touches the surface of the water. A small sample (approximately half a drop) of polymer is dipped onto the surface of the water. The polymer will begin to expand as the sample spreads out over the surface. As it spreads, the polymer will begin to show colorful patterns based on thin film interference theory. By

using the interference induced coloration on the sample, areas of constant thickness of the sample can be located. Different colors represent different thicknesses of the polymer, where areas of constant thickness can be located by areas where the color is relatively uniform. The colorful film is estimated at submicron thickness based on interference theory, whereas films several microns thick would appear to be clear. The sample is allowed to spread for a few minutes for areas of constant color to appear. When the sample has spread to an appropriate size with large enough areas of uniform color, the polymer is pre-cured for approximately 7 minutes using a UV lamp.

iii. *Create and post-cure polymer diaphragms at the end of capillary tubes.* Once the polymer has been pre-cured, the lasso is used to lift the thin layer off the surface of water. It is imperative that the layer stays flat and uniform with very few wrinkles or overlaps. An especially uniform portion (with uniform color) of the thin polymer layer is placed over a number of perpendicularly held sections of capillary tubing. The capillary tubing is then pulled through the thin layer, puncturing the layer and creating a thin diaphragm on the ends of the tubes. The capillary tubes with thin polymer diaphragms are then post-cured under the same ultraviolet lamp for approximately 1 hour to fully cure the polymer as well as strengthen adhesion between the diaphragm and the tube.

iv. *Create a mirror on the polymer diaphragm.* After the polymer diaphragm has been completely cured, a thin layer of nickel-titanium is sputtered on the outer surface of the diaphragm by using the DC Magnetron sputtering machine and

specially fabricated holder. The sputtering process is nearly identical to that of the solid-tip sensor, except a different target is used and the sputtering time is approximately 30 minutes for a reflective nickel-titanium layer of 1 µm thickness.

v. *Add additional polymer layers.* Since sputtered layers have proven to be somewhat fragile in harsh environments from previous experiments, additional polymer films are layered and cured onto the end of the diaphragm in the same manner as before in order to protect the reflective layer on the diaphragm. Additional layers can also allow for sensitivity adjustment and strengthening of the sensor should it be necessary. In the most recent fabrication attempt, 4 layers of thin polymer were added to the end of the diaphragm after the sputtered layer for protection and sensitivity adjustment. This completes the batch fabrication portion of the Fabry-Perot sensor tips, but the remaining steps can be well controlled to produce nearly identical results.

vi. *Thread the fiber into the capillary tube.* First, it is necessary to clean the excess sputtered layer off the sidewalls of the capillary tube so the fiber can be seen through the walls. The cleaved, bare fiber is inserted into the capillary tube using an actuator controlled linear translation stage. A stereo microscope is used to monitor the threading of the fiber until a given distance where it becomes difficult to distinguish the fiber end from the diaphragm; this occurs when the cavity length is roughly 40 µm.

vii.   *Fix the fiber at a desired cavity length.* Once the fiber end is no longer distinguishable, the low coherence optical system is used to monitor the cavity length obtained by using Equation (3.3). The desired cavity length is approximately 15 µm for this application, to allow for an adequate dynamic range while still retaining high sensitivity and accuracy. It should be noted that while the sensor will function properly even when the cavity length exceeds 50 µm, the sensitivity and the accuracy suffer with increased cavity lengths. Using the optical system to monitor the cavity length, when the exact desired length is met, the fiber is fixed into place with the epoxy at the non-sensing end of the tube. Similar to the solid-tip sensor, since the fiber was stripped slightly longer than the length of the capillary tube, there is a portion of bare fiber than extends beyond the capillary tube. Additional epoxy is used to coat the rest of the bare fiber extending outside the tube for strengthening purposes. If the extending bare fiber is too long, a protective jacket or tube can also be used to cover the bare fiber portion. The process of fiber insertion and cavity length manipulation is shown in Figure 3.11.

viii.   *Create a connector on the free end of the optical fiber.* Finally, the last step to complete the sensor is to create a connector on the free end of the optical fiber.

Following the steps mentioned above yields a repeatable sensor fabrication process. Alternatively, changing the materials and/or the procedures will allow one to customize the sensor performance properties. Images of the sensor during the fabrication process are illustrated in Figure 3.12, and an image of a completed Fabry-

Perot sensor constructed by utilizing the above mentioned procedure is shown in Figure 3.13. The center circle is the deformable diaphragm, while beyond that circle are the capillary tube walls.

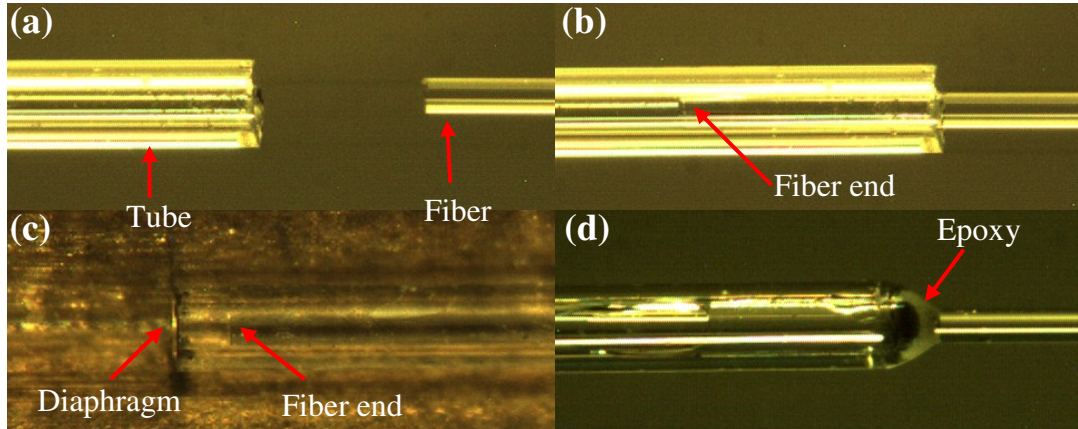Figure 3.12: Photographs of the fabrication process: (a) fiber and tube aligned with stage, (b) fiber inserted into tube, (c) fiber threaded toward diaphragm, and (d) fiber fixed with epoxy.
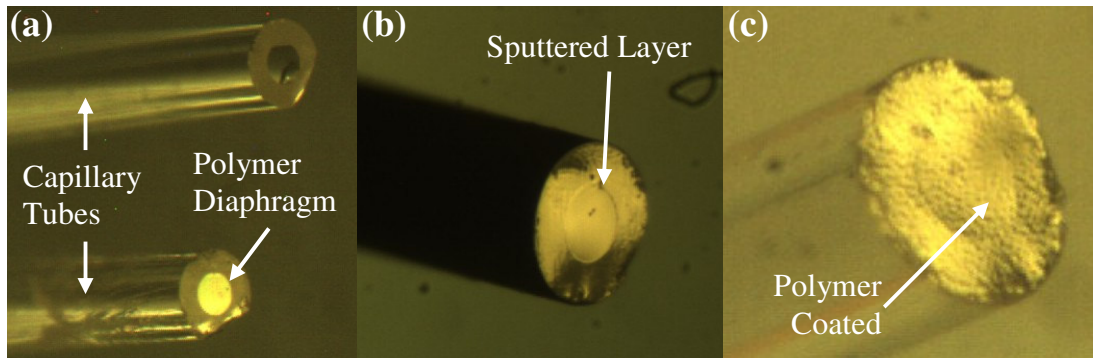

Figure 3.13: Photographs of sensor structure: (a) cleaved tubes with and without polymer diaphragm, (b) diaphragm with sputtered Ni-Ti layer, and (c) sensor tip with cleaned sidewalls and added protective polymer layers.
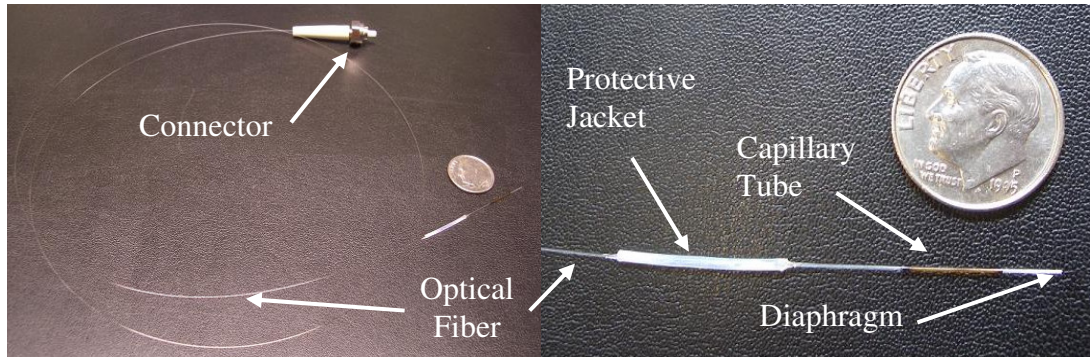
Figure 3.14: Completed Fabry-Perot sensor.

3.2.3 Summary of the Fabry-Perot Sensor Design

This type of sensor design and fabrication has many advantages when compared to other designs. As mentioned in Section 3.1.3, a thin diaphragm, while being more fragile to harsh environments and high pressures, will allow for a greatly increased sensitivity to pressure. As long as the applied pressure from the experimental testing does not exceed extreme values, the Fabry-Perot sensor should be reusable for several pressure tests, and one should be able to get repeatable results. Rather than silicon or silicon dioxide, which is commonly utilized for miniature diaphragm based Fabry-Perot sensors, a polymer material is used due to its biocompatibility, high flexibility, and ability to yield without failing. Silicon is generally very brittle, and hence, it often results in a catastrophic failure rather than yielding when mechanical stresses exceed the critical limits.

Another very significant benefit to this sensor design is the response time. Since dynamic pressure measurements are required for in-tail testing, in order to obtain accurate pressure readings, a sensor with enough response time is necessary. Since this design employs a thin diaphragm that has a short response time to the pressure changes than that of the solid-tip sensor, the diaphragm based sensor is

expected to perform better in dynamic pressure measurements. Furthermore, this design allows for easy adjustment of the sensitivity. The sensitivity can be controlled simply by increasing the thickness of the diaphragm by sputtering for a longer period of time or by adding a higher number of polymer layers. These added layers can also help protect the sputtered layer from reflectivity degradation when exposed to biological tissues.

In addition, this design and fabrication procedure is amenable to batch fabrication. Since the majority of the steps can be performed with a batch of sensors, this can help achieve good device uniformity, rendering sensors with similar characteristics such as sensitivity, resolution, and linearity.

In the fabrication process, there are a few steps with minor difficulties that should be noted. Firstly, when pre-curing the polymer for the diaphragm, it takes some experience to determine exactly how long the polymer should be exposed to the UV lamp, and whether the film is solidified enough to transfer onto the tubes. A certain level of solidification is needed to manipulate the film with the lasso without any tears or wrinkles while still remaining soft enough to be easily punctured by the capillary tubes. In the experiments, it has been found that an approximate cure time of 7 minutes works well, the cure-rate can vary depending upon the polymer material's thickness and distance from the UV lamp. Secondly, the fiber insertion step has some associated difficulties as well. In order for the fiber to fit and travel smoothly through the capillary tube, it is essential for the translation stages to be properly aligned. Depending upon the length of the fiber being threaded, great resistance can accumulate through friction or bending as the fiber goes deeper into the

tube. If the fiber gets jammed, the large forces can potentially cause the fiber to jump an uncontrollable distance (often tens of micrometers) as soon as the force exceeds that of the static friction. This makes it difficult to achieve the desired cavity length of only 15 µm.

Chapter 4: Experimental Study of Miniature Fiber Optic Pressure Sensor Systems for *In Vitro* Intradiscal Pressure Measurements of Rodents

This chapter contains details of the experimental studies conducted on the two fiber optic sensor systems developed in this thesis work. These studies include preliminary tests, *in vitro* intradiscal pressure measurements of rodent tails, and calibration experiments. A summary of sensor performance and observations are also provided.

4.1 Experimental Arrangement

The experimental setup utilized for intradiscal pressure measurements was a slight modification of one devised for rodent motion segment loading tests by Professor Hsieh's Orthopaedic Mechanobiology group in the Department of Bioengineering.

A motion segment of a rodent tail consists of an intervertebral disc enclosed by two vertebrae and isolated from all surrounding soft tissues. This surgery was performed before the experiments by the staff in Professor Hsieh's group. Different discs throughout the tail have different properties. The choice of which disc to test as well as what test to perform are not the focus of this thesis work, which are carried out by Professor Hsieh's group.

For the experimental setup, a motion segment containing the rat disc of interest is mounted onto a materials testing system by using micro-vises; the two vertebrae surrounding the disc are fixed into the micro-vises with bone cement.

Compressive loads are applied externally by the Enduratec loading mechanism to generate pressures within the rat tail disc. The loading and displacement data are recorded by using the Enduratec system's data acquisition card (DAQ), which is connected to a computer. Here, the loading is referred to as the force applied by the actuator, while the displacement is the compressive displacement of the motion segment experienced along the vertical axis.

Accommodating this setup to allow for intradiscal pressure testing requires little modifications. Since the fiber optic sensor system is independent of the Enduratec system, data are either recorded manually or acquired by using the SpectraSuite Spectroscopy Platform Software onto a laptop, and then, matched up with the load and displacement data accordingly. The sensor is held in a 3-dimensional translation stage fixed onto the breadboard behind the tail specimen, where the sensor can be carefully positioned to be at the center of the rodent tail disc. The typical experimental setup utilized for disc loading tests is shown in Figure 4.1.
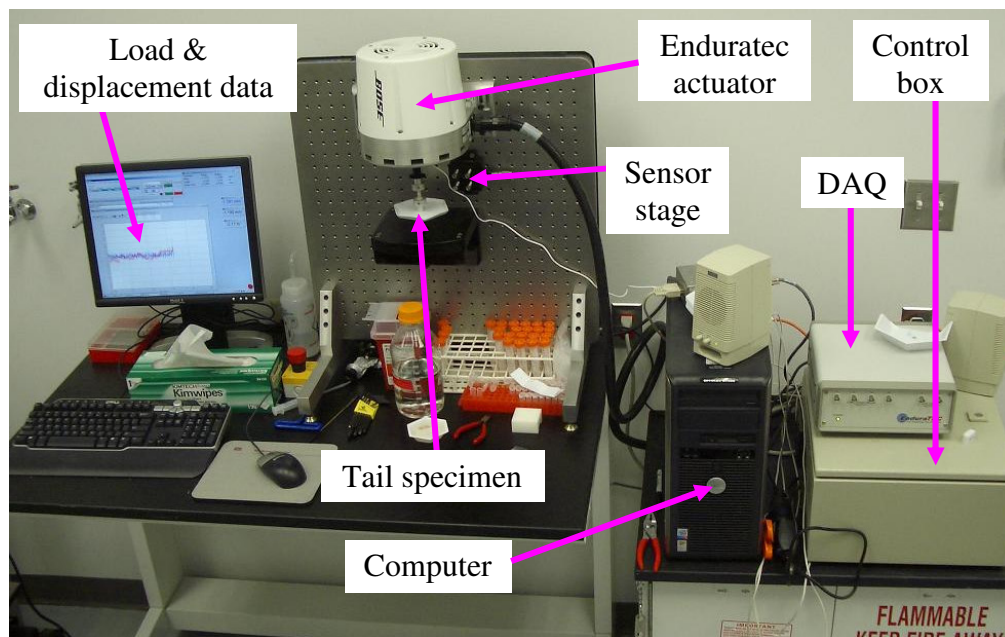

Figure 4.1: Experimental setup for *in vitro* disc loading.

Specific procedures are followed when inserting the miniature pressure sensor into the disc to avoid any damage to the disc as well as to the sensor. A 22 gauge hypodermic needle is used to puncture the disc to the center depth and create a hole for the sensor to be inserted. Previous tests conducted by Prof. Hsieh's group have shown that this action causes minimal disturbances to the disc structure [7]. The needle is then withdrawn and the sensor is positioned at the exact location of the hole and inserted into the center depth by using the 3-dimensional translation stage. An image of a sensors successfully inserted into a rodent disc can be seen in Figure 4.2 and Figure 4.3.

As shown in Figure 4.2 and 4.3, the lower micro-vice is used to fix the motion segment in place, while the upper vice is attached to the Enduratec actuator that acts as the loading mechanism. This system allows for the following modes of testing: i) displacement controlled mode and ii) load controlled mode. Since the motion segments are viscoelastic, load and displacement values will not necessarily match up. Instead, loading of the disc will cause creep, decaying trends, and a gradual shift toward equilibrium. Thus, this testing mechanism uses an open loop controller to maintain the displacement at a constant value or follow a prescribed trend, or it can also control the load in a similar fashion. Both the displacement and loading data are monitored and recorded to get a better understanding of the state of the disc.
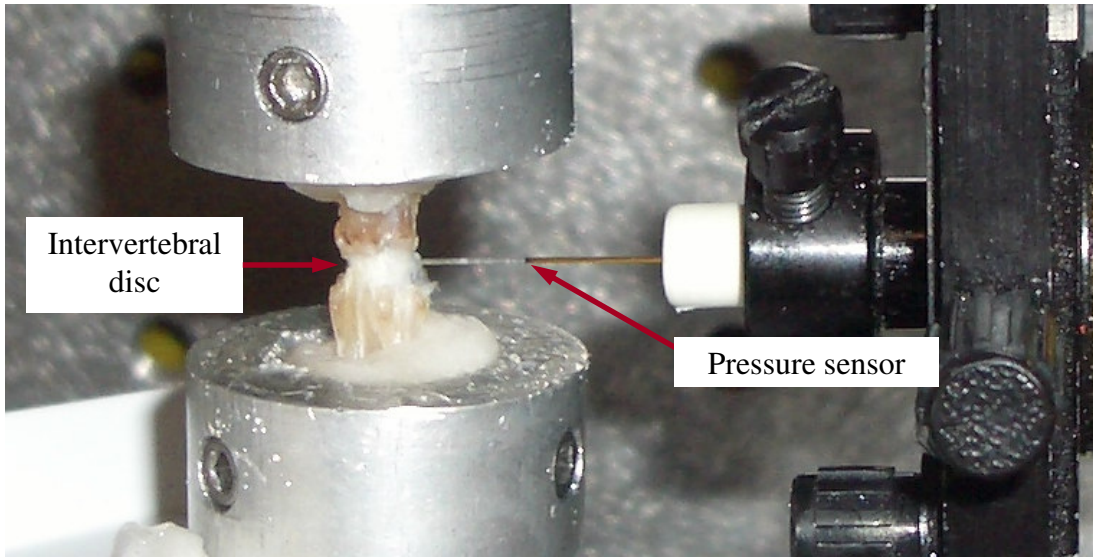
Figure 4.2: Fiber optic sensor inserted into the center of the rat tail disc.
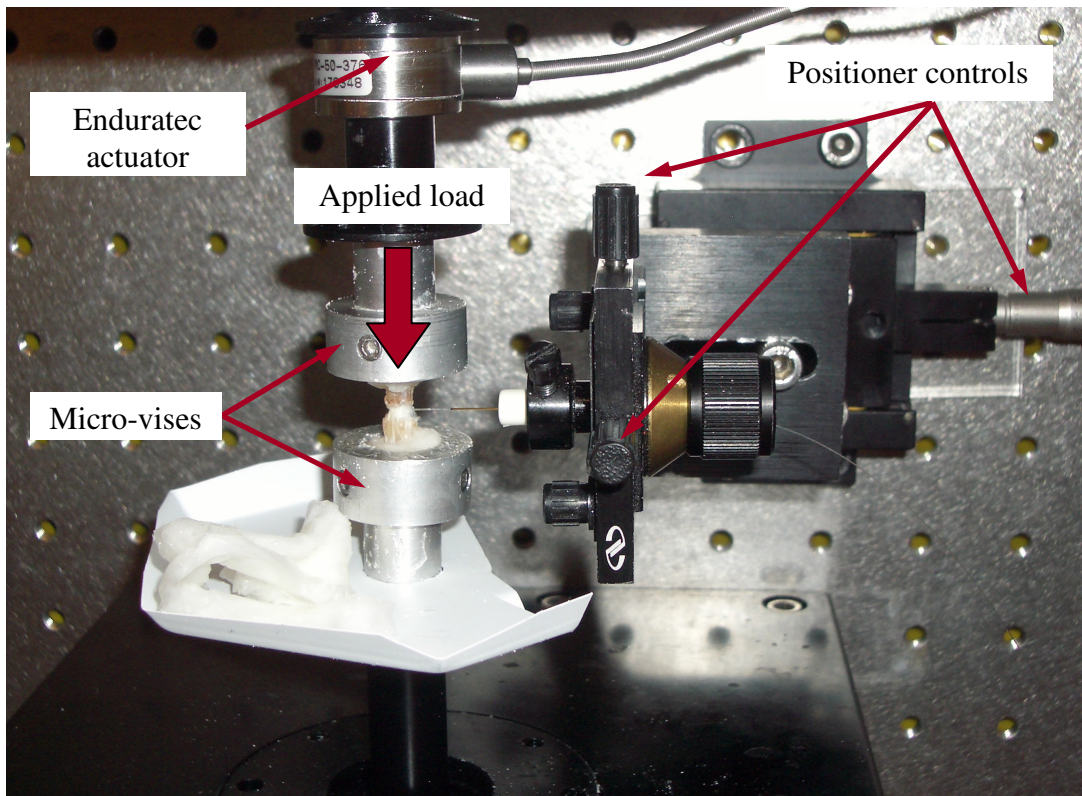

Figure 4.3: Experimental setup for intradiscal pressure test.

4.2 In Vitro Intradiscal Pressure Measurements Using Intensity Based Solid-Tip Sensor

4.2.1 In Vitro Intradiscal Pressure Measurements

Preliminary intradiscal pressure testing was conducted by using the intensity based configuration and solid-tip sensor design described in Chapters 2 and 3, respectively. The purpose of these preliminary tests was to verify the sensor was capable of sensing pressure variations. Since the sensor was not calibrated prior to the in-tail testing, specific pressure values cannot be attributed to the testing results. However, the testing does allow for an analysis of general correlations.

Once the optical sensor was inserted into the rodent disc, following the procedures described earlier, two separate tests were conducted to observe the pressure variation as well as the sensor's performance. Both test routines were selected by the Orthopaedic Mechanobiology group based on precedents of disc testing methods. The first experiment was a displacement controlled test, where a constant compressive displacement was applied to the disc for 30 seconds, then the displacement was increased a step, and this pattern was repeated for approximately 3 minutes. The first three displacements had a step increase of 0.1 mm, while the final step compressed the motion segment 0.2 mm further. The sensor readings from the power meter were manually monitored and recorded every 5 seconds. After the tests, the sensor data was matched up with the corresponding displacement and load values based upon the corresponding times of each step of compression.

The results recorded from the displacement controlled test, are shown in Figure 4.4. In this figure, the time history of the displacement, load, and optical

62

sensor data are plotted. When comparing the load and displacement data taken by the Enduratec system, at each incremental step of compression, the load exerted by the system starts with a large value and then gradually decreases as the disc approaches equilibrium. This indicates that less force is required to maintain the same compressive displacement; a viscoelastic behavior of the disc is observed, which is expected. From the figure, it can be seen that the optical sensor showed an increase of optical power with respect to each compressive step. Thus the preliminary test results showed a distinct correlation of an increase in the disc pressure with respect to a greater compression. It should be noted that the first few step increases in optical power occur slightly before the compressions of the disc. This may be due to the mismatch of the optical data with the other data, as the data was recorded manually and matched up with load and displacement data afterward.
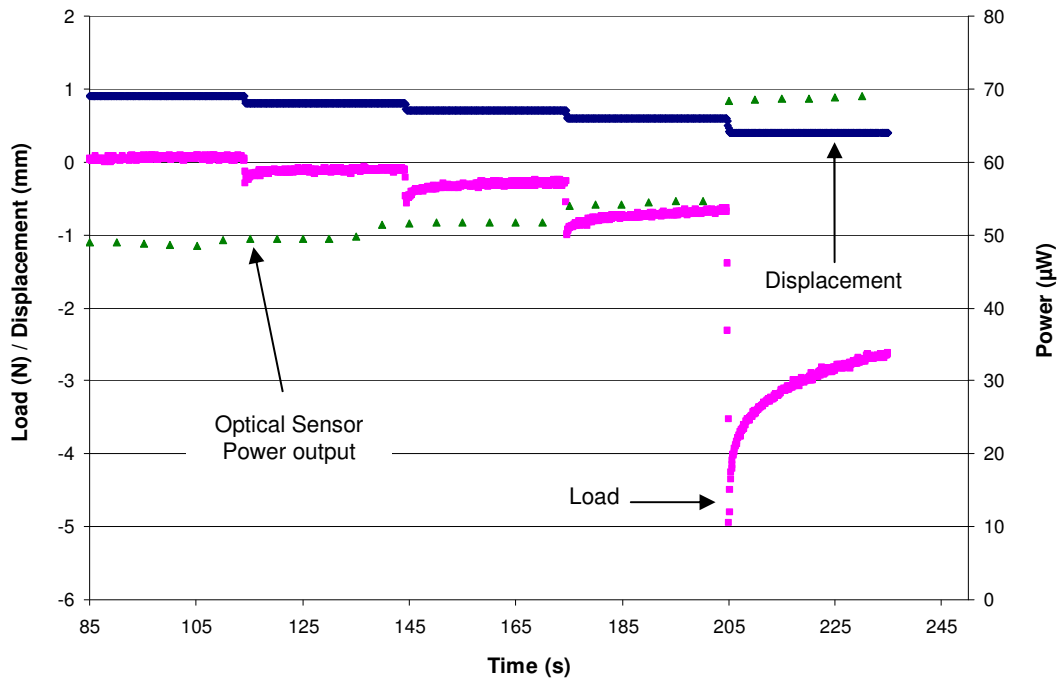
Figure 4.4: Experimental results from a displacement controlled test with solid-tip sensor.

Another in-tail test was performed with a different solid-tip sensor by utilizing the load controlled method. In this test, a constant load was applied for 30 seconds followed by a release for 30 seconds, and this pattern was continued with amplified loads for 7 cycles. Again, the sensor readings were taken manually every 5 seconds and correlated with the displacement and load values after the test.

The results recorded from the load controlled test are shown in Figure 4.5. Again, time histories of the displacement, load, and optical sensor data are plotted. The displacements and loads from both tests are shown to have similar magnitudes. Additionally, from Figure 4.5, possible viscoelastic behavior is exhibited through the gradual increase in displacement under a constant compressive load. The optical power output was not recorded for the first several cycles of loading. However, from the optical data that was recorded, a fairly distinct correlation of gradual increase and decrease of the optical power can be seen in each loading cycle.
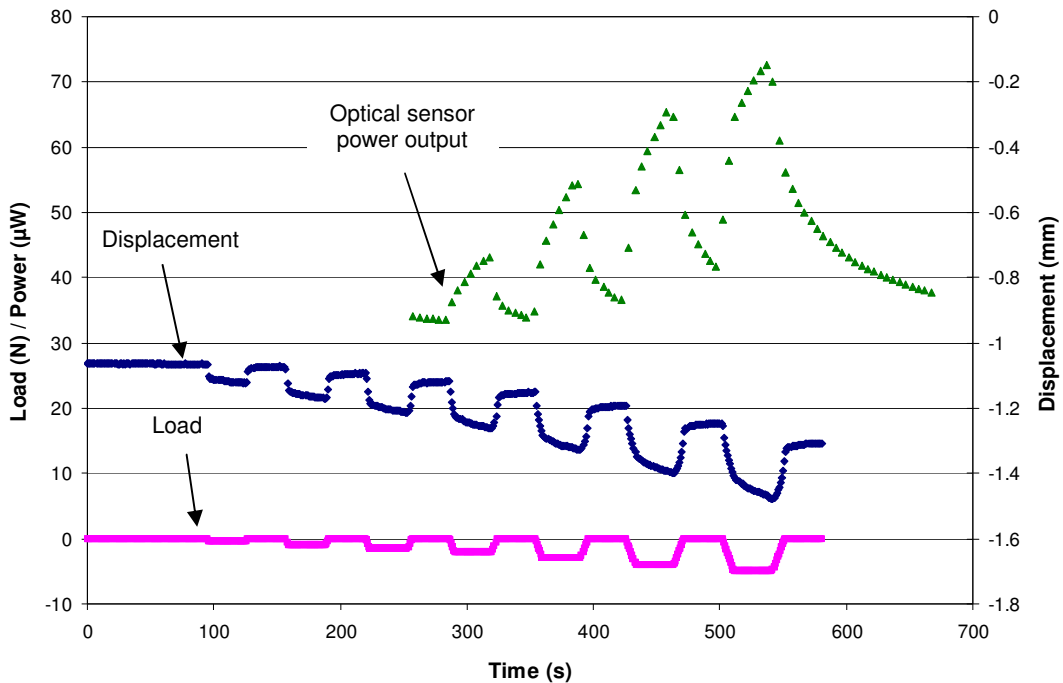

Figure 4.5: Experimental results from a load controlled test with solid-tip sensor.

4.2.2 Summary of the Intensity Based Solid-Tip Sensor Performance

By using the intensity based optical system with a solid-tip sensor, good correlations of changes in optical intensity with an applied loading/displacement have been observed from both displacement controlled and load controlled in-tail tests. Since the sensors utilized were yet to be calibrated, the resulting optical power values cannot be converted into actual pressure values. However, these tests successfully demonstrate that the intensity based solid-tip sensor is capable of sensing the magnitudes of pressures within the rat disc.

Many characteristics of the sensor must be considered after examining the test results. The results are substantial in validating the sensor system with a good correlation of light intensity change corresponding to a pressure variation under applied loads and displacements. However, since there is no precedence in intradiscal pressure measurements of rodents, it is impossible to determine whether the sensor's output intensities accurately portray the pressures within the disc. Without having the sensor calibrated, the details of the performance parameters of the sensor system cannot be obtained. Thus, while the sensor shows a promising general trend and the capability of carrying out intradiscal pressure measurements, it is unknown whether the sensor's characteristics such as the response time and resolution are adequate for this application.

The response time of the sensor, which refers to the time it takes for the sensing component to react to a variation in pressure, is an important characteristic that must be known in order to accurately capture the dynamic pressures within the rodent disc. Since the solid-tip sensor design has a large deforming region of

approximately 60 µm, the deformation rate of the polymer can be a major issue. As previously stated, the rodent tail disc demonstrates viscoelastic behavior; as the fluid within the disc flow toward equilibrium, it is expected that the pressures within the disc will fluctuate as well. Therefore, the sensor must be capable of sensing and characterizing these rapid changes in the internal pressure. For example, from results obtained from the load controlled test shown in Figure 4.5, it is impossible to determine whether the exponential characteristics of the increase and decay of the intensity are due to the pressures within the disc or the sensor's response time. While the data was only taken manually every 5 seconds, future tests for creep of the disc would require the use of a faster photodetector and a sensor with a faster response time.

It was found that both solid-tip sensors were no longer functional after several days followed their respective in-tail tests. A study was carried out to find out the reasons for their failure. Two major problems were identified for the solid-tip ends. First, the sensor's polymer ends exhibited a much higher stiffness than that during the in-tail testing. This stiffening can likely be attributed to further curing of the polymer end. When fabricated, the polymer is only partially cured until just solidified to remain as elastic as possible. The in-tail testing was executed soon after the fabrication of the sensors was complete. After inserting the sensors into the discs and letting them sit for several days, the polymer continued to cure naturally so that it became stiffer and less sensitive to pressures.

Another severe problem that was discovered was the destruction of the sputtered layer. Without the sputtered layer to reflect the light back into the power

meter, the intensity based sensor loses its functionality. On closer inspection, a possible peeling or deterioration of the sputtered titanium layer was found, which can be seen in the photographs shown in Figure 4.6. The tip of the sensor-end becomes translucent and glossy compared to the rest of the sensor, which is covered in sputtered titanium. The loss of the titanium layer could be due to many causes. It is possible that the titanium has poor adhesion to the polymer and that the convex shape of the polymer end contributes to peeling of the sputtered layer. It may also be the pressurized liquid environment within the disc causes a deterioration of the sputtered layer. Any combination of the three would be plausible reasons for the destruction of the sputtered mirror.

Figure 4.6: Photograph of the deterioration of the sputtered layer after in-tail testing.

Based on the test results and observations afterward, it is clear that some improvements need to be made to the sensor and the optical system. There is much room for improvement for the optical sensing system, since an intensity based sensing system is a simple approach. It would be quite beneficial to use an upgraded system that has a high sampling rate, increased sensitivity, and exhibits robustness to possible fluctuations. The solid-tip sensor also needs to be improved, especially with the

issues of the destruction of the sputtered layer and the low response time of the solid polymer tip.

4.3 In Vitro Intradiscal Pressure Measurements Using Low Coherence Interferometry System with Diaphragm Based Fabry-Perot Sensor

4.3.1 Preliminary Study of the Sensor System

Preliminary pressure tests outside of the rodent tail segments were conducted to validate the Fabry-Perot pressure sensor and the optical system. In the experiment, compressed air was directed toward the diaphragm of the Fabry-Perot sensor to generate a dynamic pressure. The sensor was tested with a gradual application, release, and re-application of small pressures while the spectrum reading was recorded every 100 ms for 20 seconds. During the experiments, the peaks in the reflected spectrum showed significant shifts with respect to the deformations of the diaphragm. The interference fringes obtained from the spectrometer showed good visibility for determining the subsequent cavity lengths due to the deflection of the diaphragm. Two fringe spectra obtained during the pressure test are compared in Figure 4.7. The cavity length of the sensor in ambient pressure was obtained to be approximately 23.84 µm based on the demodulation of the spectrum seen in Figure 4.7(a), while with applied pressures, the cavity length dropped to 23.30 µm based on Figure 4.7(b).

MATLAB programs, which are included in Appendix A, were developed to obtain the average as well as the standard deviation of the cavity lengths for the spectrum readings throughout the test. The obtained average cavity lengths are

plotted as a function of time in Figure 4.8. This preliminary test shows the sensor responds well to small dynamic pressures. The somewhat erratic change in cavity length can be correlated to the application and release of the arbitrarily applied pressure with the simple goal of verifying an expected response. In these tests, a sampling rate of 10 Hz was achieved without difficulty. Greater sampling rates can be achieved by improving the interference visibility and decreasing the integration time during data acquisition.
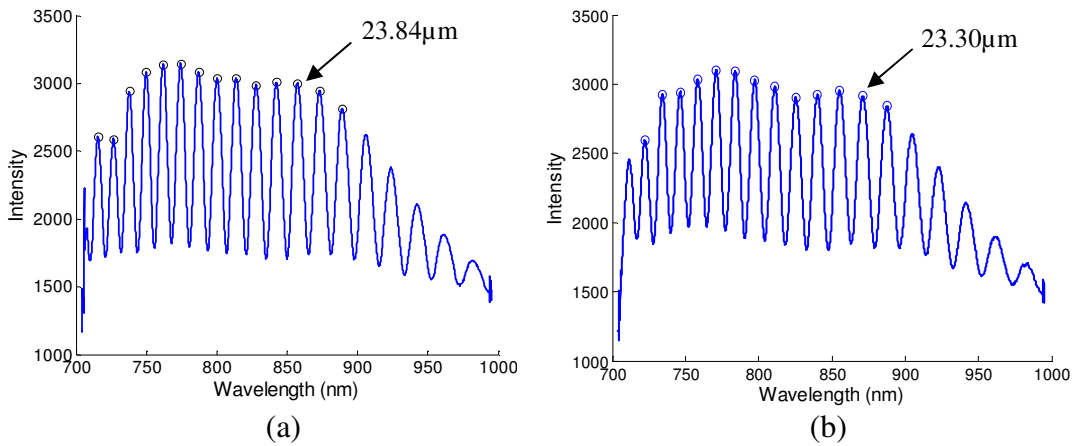

(a)   (b)

Figure 4.7: Reflected spectrum from the sensor: (a) at ambient pressure and (b) with a small applied pressure.
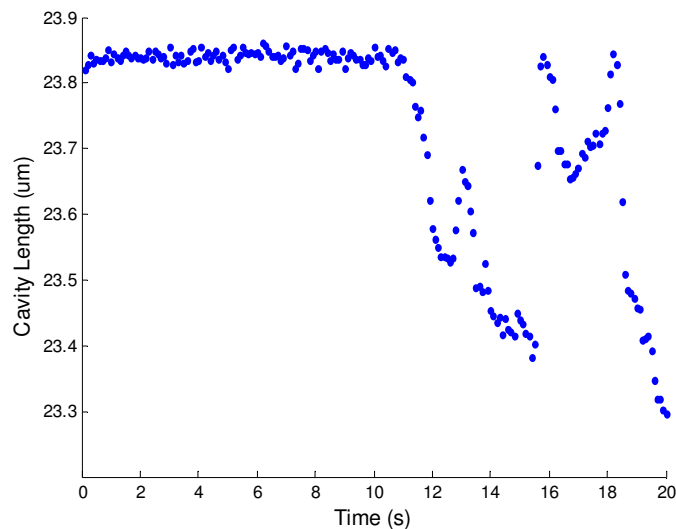

Figure 4.8: Change in cavity length over time during preliminary pressure testing.

69

4.3.2 Sensor Calibration

Sensor calibration was conducted to quantify the changes in cavity lengths with respect to applied pressure variations. A pressure chamber fabricated from a plastic bottle was utilized for the calibration tests. The arrangement of the calibration experiment is shown in Figure 4.9. A commercially available sensor made by Kulite Semiconductor Products was used in the calibration. The Kulite sensor utilizes a 10 V DC power source, and the output voltage corresponding to pressures is on the millivolts scale with a sensitivity of 4.068 mV/psi.

Both the Kulite pressure sensor and the Fabry Perot pressure sensor were placed inside the chamber to expose them to the same pressure conditions. Based on the readings from the Kulite sensor, the pressure in the chamber was first increased to approximately 10 psi and then gradually released. During this process, pressure readings from the Kulite sensor and the cavity length measurements of the Fabry-Perot sensor were recorded simultaneously. The obtained pressure calibration results are shown in Figure 4.10.
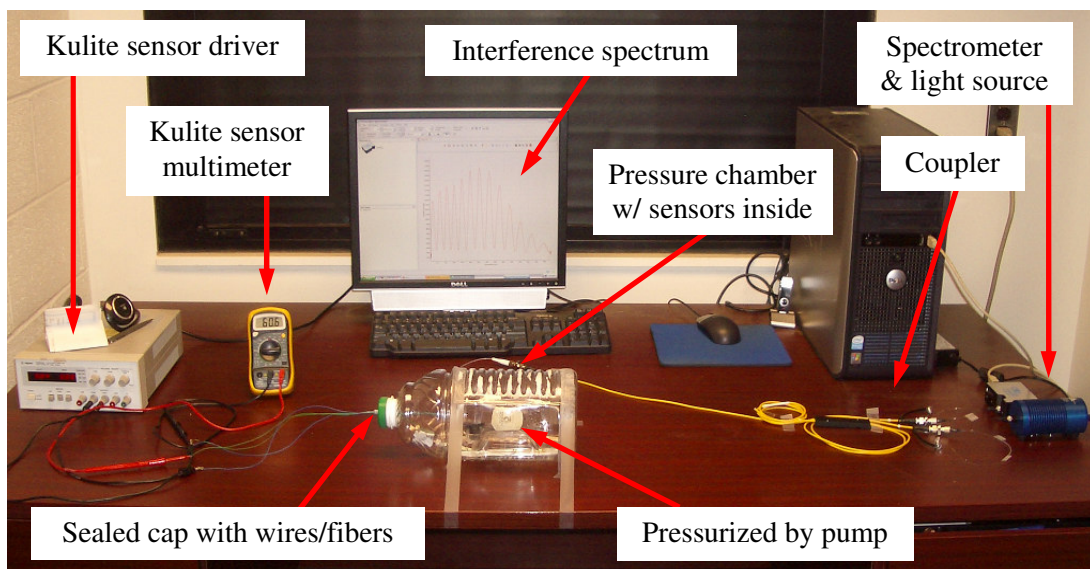
Figure 4.9: Experimental arrangement for sensor calibration.
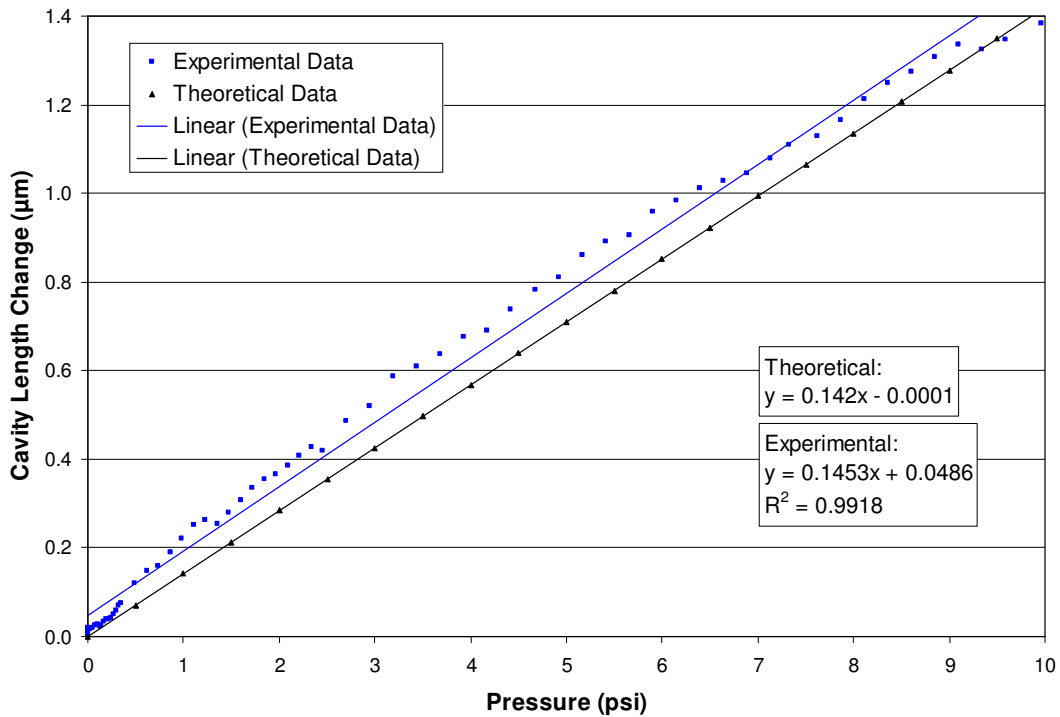
Figure 4.10: Sensor calibration curve.

Based on the calibration results, the curves obtained from the analysis in Chapter 3 were matched to find the best fit. The analysis for a circular clamped diaphragm of 1.3 µm thickness was found to have the closest fit to the experimental data. The sample coefficient of determination R^2, which is a statistical regression analysis measure that assesses the quality of a trendline, was used to determine the linearity of the sensor. The sample coefficient of determination is defined as [37]

$$R^2 = 1 - \frac{\sum (Y - \hat{Y}(X))^2}{\sum (Y - \bar{Y})^2} \qquad . \qquad (4.1)$$

The closer this value is to 1, the better the fit of the trendline. The sensor tested showed good linearity as seen by the R^2 value of 0.9918. Similar to the results

obtained from the analysis, the sensitivity of the sensor obtained from the slope of the calibration curve was found to be 0.14 µm/psi.

Based on the experimental results, the minimum detectable pressure (pressure resolution) was found to be less than 0.025 psi. However, due to the relatively large noise floor of the Kulite sensor, the exact resolution of the Fabry-Perot pressure sensor could not be obtained. A digital multimeter was used to read the output voltage from the Kulite sensor, which has an accuracy of a tenth of a millivolt. Thus, the pressure resolution of the Kulite sensor system is limited to 0.025 psi. Even for a pressure change corresponding to a multimeter reading of 0.1 mV for the Kulite sensor, the optical sensor is capable of detecting the change, thus showing a minimum detectable pressure better than the Kulite sensor with the multimeter reading.

By further examining the calibration curve, additional observations about the sensor can be made. An examination of the data from pressures below a pressure level of 6 psi shows the sensor has slightly better linearity with the R^2 value of 0.995 and slightly increased sensitivity of 0.16 µm/psi, as seen in Figure 4.11.
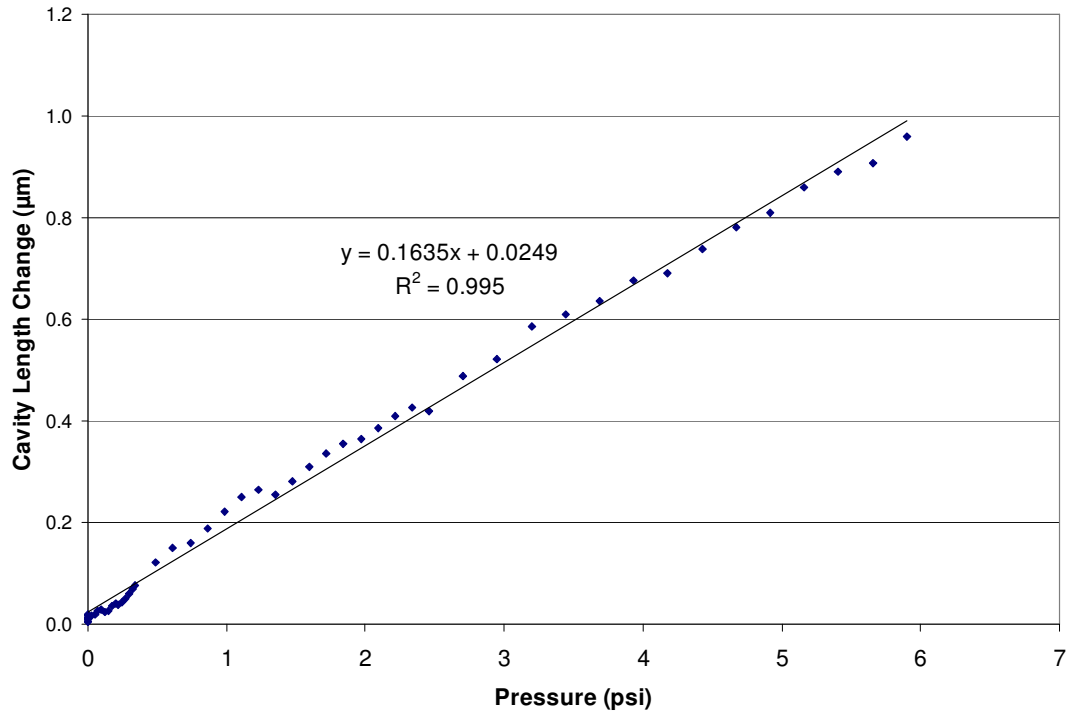
Figure 4.11: Linearity for a section of data from calibration experiment.

4.3.3 Creep Testing

In addition to the calibration test, a creep test was also conducted to better understand the sensor's response time. An initial pressure of approximately 10 psi was held for about a minute and then released while the sensor's readings were recorded. The data recorded by the pressure sensor system during the creep test is shown in Figure 4.12. From the time the pressure was released, it took 5 seconds for the cavity length to reach within a 10% range of the expected cavity length in atmospheric pressure, and 14 seconds to reach within a 5% range. This does not account for the time it took for the pressure to return to the atmospheric pressure after release, which is expected to take no more than a few seconds at most. The delay in the sensor response is likely due to the drastic change in pressure in such a short time.

During such a short time, it is possible that the polymer diaphragm responds slower than the pressure drops due to the fact that it requires some time to return to an un-stretched state. In the actual intradiscal pressure tests, due to the viscous effects of the tissue, it is expected that sudden pressure changes of this magnitude would not occur.
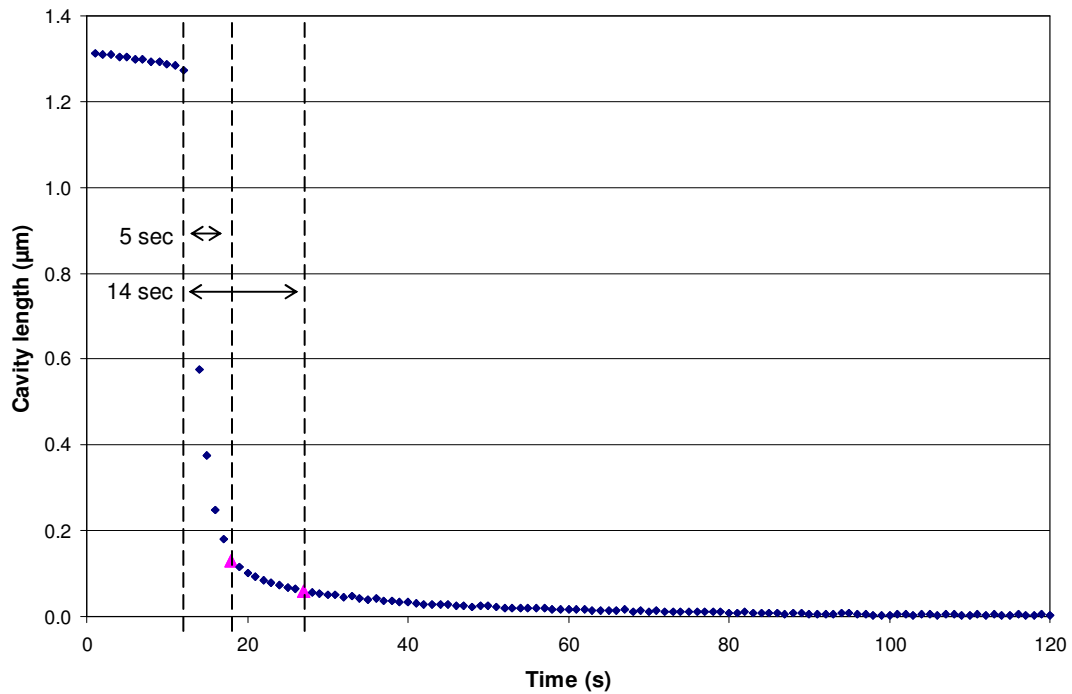
Figure 4.12: Creep test results.

4.3.4 In Vitro Intradiscal Pressure Measurements

A preliminary intradiscal pressure experiment was conducted to verify that the Fabry-Perot sensor can effectively detect the intradiscal pressures generated from externally applied loads. This test was conducted prior to calibration studies, and the sensor broke shortly after the in-tail test was completed. The results obtained from this test are provided in Appendix B1. Although the sensor was found to be too

sensitive, not durable enough, and experienced permanent deformation, this test gave insight into the required thickness of the diaphragm needed to have an appropriate sensitivity for intradiscal pressure measurements in rodents.

Following the preliminary test, a new sensor was fabricated with a thicker diaphragm that includes more layers of the protective polymer material. This is the sensor that was used for calibration studies. After the performance properties of the sensor were established, the calibrated sensor was utilized in the intervertebral disc testing with the aim of quantitatively measuring the intradiscal pressures generated due to the externally applied loads. The pressure test was similar to the displacement controlled test conducted for the solid-tip sensor, but with a smaller step size and a larger number of them. During the approximate 6 minutes test, 0.05 mm of compressive displacement was added at each step except for the last step, which was 0.1 mm. Each step was held for 1 minute before applying more compression and the test ended after 0.5 mm of total displacement. The displacement, load, and cavity length results obtained from the test are shown in Figure 4.13. It was found that the newly made, calibrated sensor had deformations exceeding expectations. Due to the limitation of the pressure chamber, the sensor was only calibrated to approximately 10 psi (corresponding to approximately 1.4 µm of deformation). Thus, it is unknown whether the sensor maintains a good linearity beyond the pressure of 10 psi and the corresponding pressure values that induce a diaphragm deformation greater than 1.4 µm remain unknown. However, pressure values can be obtained for the first few steps of the test before pressures exceeded 10 psi; this is shown in Figure 4.14.
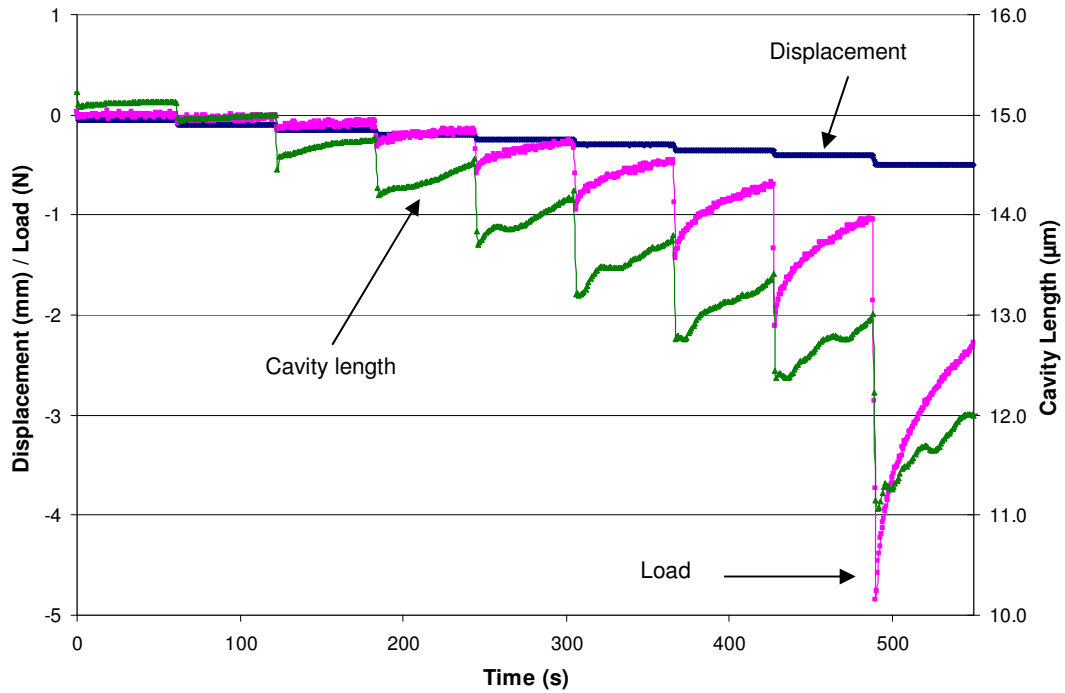
75

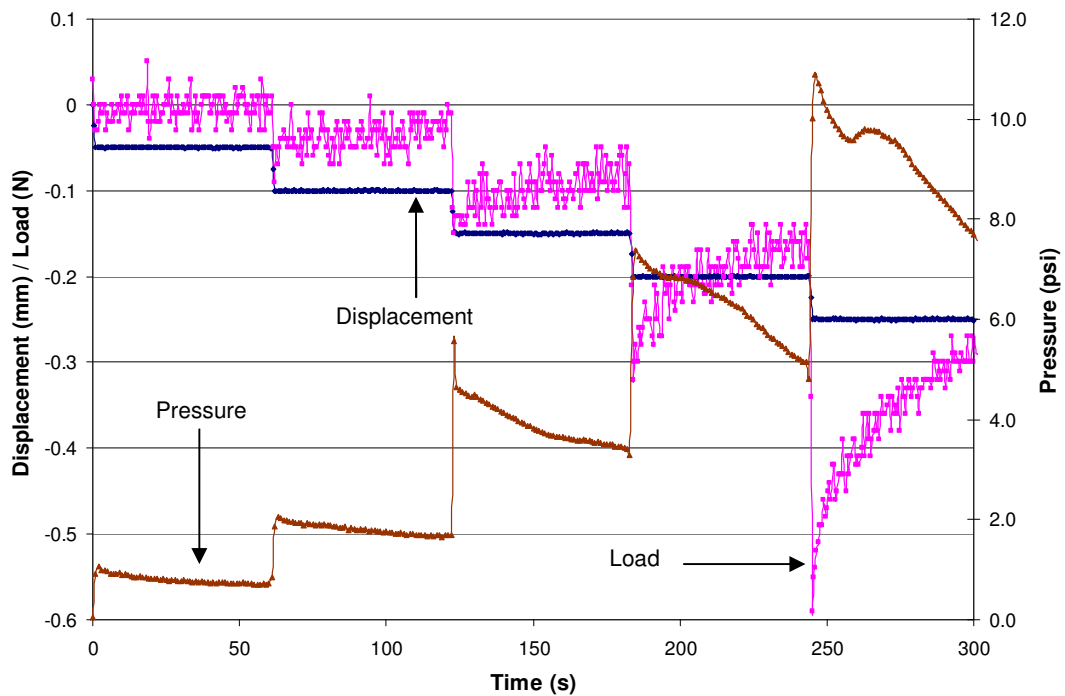Figure 4.13: Pressure sensor response to the quantitative intervertebral disc pressure test.

Figure 4.14: Intradiscal pressure measurement results corresponding to pressure values below 10 psi.

From Figures 4.13 and 4.14, one can see that the pressure sensor, while perhaps still too sensitive for rodent disc studies, shows an excellent response to the applied loads with only noise. The visibility of interference pattern was exceptional, with standard deviations between 3%-6% throughout the entire test.

In Figure 4.14, a much steadier pressure sensor response below 10 psi than that of the Enduratec system's load measurement device is shown. For these first few compression steps, the load magnitudes were so small that the noise from the Enduratec system was significant, while the pressure sensor showed a smooth response to the pressure magnitudes with much less noise.

A second in-tail experiment was performed shortly following the first test to verify repeatability. The corresponding results are provided in Appendix B2 and B3. Results from the second test showed very similar responses to that of the first test. When compared to Figures 4.13 and 4.14, it can be seen that in the second test, the disc began to show a change in response to the applied compression. For the same compression, smaller load and pressure values were obtained from the second test than those obtained from the first test.

Some further study of the results can reveal information about rodent disc pressures that are yet unknown. Although a careful study with various tests would be necessary to draw substantial conclusions, one can still analyze the data to determine general trends regarding the relationship between the disc pressures and the externally applied forces. In Figure 4.15, the load and pressure values are compared specifically during the 5th compressive step. This step is chosen because the loads are large enough to overcome the noise experienced by the load measurements, and because it

is the last step that remained mostly within the calibrated pressure regions of the sensor. As shown in Figure 4.15, a quasi-linear relationship between the load and pressure with some transient fluctuation can be observed. While further validation is still needed, this is a promising discovery towards understanding of the behavior of rodent discs under externally applied loads.
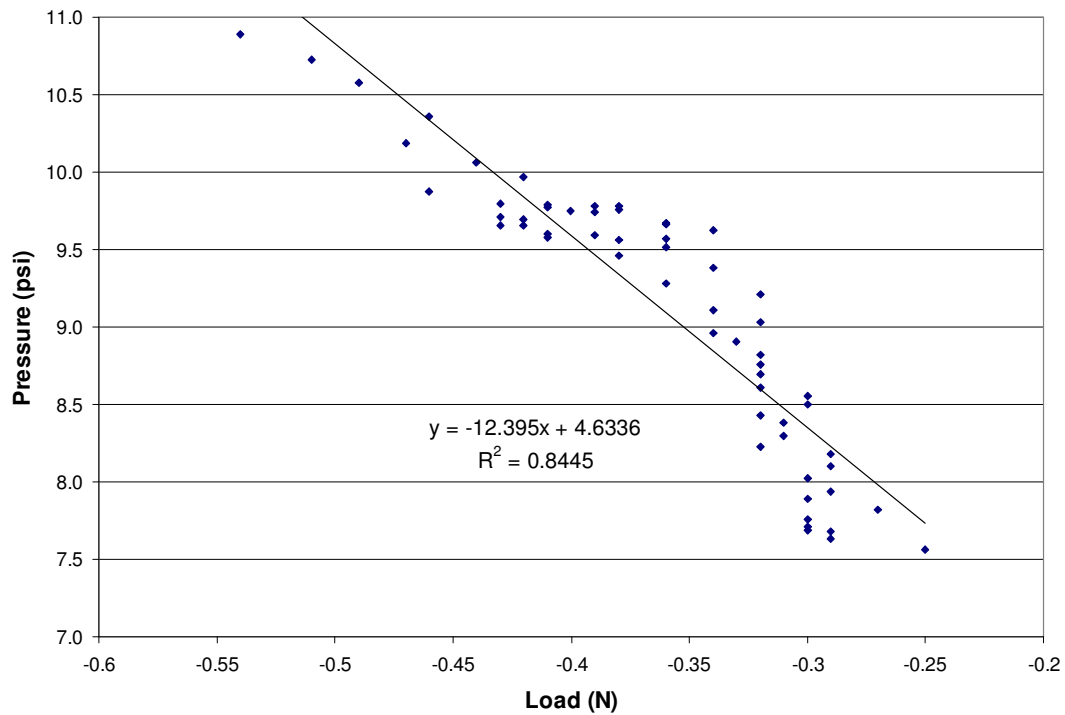
Figure 4.15: Comparison of load and pressure during the 5th step.

4.3.5 Summary of the Low Coherence Interferometry based Fabry-Perot

Sensor Performance

The multi-layered diaphragm based Fabry-Perot sensor shows great promise as a miniature fiber optic pressure sensor for intradiscal pressure measurements of rodents. It has been proven that both the sensor and the sensing system are capable of detecting small pressures within the rodent disc generated from applied loads and

displacements. In the experiments, the sensor system maintained a very good signal visibility even under large applied pressures. Furthermore, the sensor could be used with excellent repeatability and the cavity length is seen to be maintained before and after the pressure tests. Additionally, unlike the solid-tip design, the sputtered layer remained intact despite the pressure tests within the rodent disc, and thus, the sensor remained functional even after the tests. The Fabry-Perot sensors are also very inexpensive to construct and can be mass produced with varying properties. In general, by using the diaphragm based Fabry-Perot sensor along with a low coherence interferometric sensor interrogation system, the problems associated with the intensity based solid-tip sensor are successfully addressed. Despite nonlinear effects and creep effects, the sensor still shows great potential for the considered application.

Despite the promise of the low coherence interferometry based sensor system, some drawbacks still exist. In order to achieve better performance properties, this sensor system is much more complex than the intensity based system. The complexity of the system also results in a much higher cost for the system compared to the intensity based system. In addition, since the cavity length changes can only be obtained from indirect measurements of the interference fringes, a real time measurement cannot yet be realized.

Chapter 5: Conclusions

In this chapter, this thesis research is summarized. In addition, the contributions made in this thesis and future research directions are also discussed.

5.1 Summary

In this research, the goals were the following: i) to develop an optical sensor system capable of quantifying small pressure variations, ii) to design a reliable, miniature sensor for measuring pressures within the intervertebral discs of rodents without adversely disrupting the structure, iii) to establish a repeatable fabrication process to construct the sensor, and iv) to verify the sensor's performance capabilities through intradiscal pressure experiments in rodents. The thesis efforts can be summarized as follows:.

- Two different fiber optical sensor systems have been developed: one being an intensity based sensor system and the other being a low coherence interferometry based sensor system. The intensity based system employs a simple design that utilizes an SLD light source to illuminate the system and a power meter to measure the pressure induced variations in light intensity. Although the system has a simple design, this system intrinsically suffers from various power fluctuations and drifts. The low coherence interferometry system utilizes a broadband light source for illumination and a high speed spectrometer with specialized software to obtain the pressure induced light interference changes in the spectral domain. It has many advantages over the intensity based system, which include high sensitivity, high resolution, large

dynamic range, and immunity to all kinds of power fluctuations and wavelength fluctuations of the light source.

- Two different miniature fiber optic pressure sensors have been designed, developed, and fabricated for use along with the sensor systems: a solid-tip intensity based sensor and a diaphragm based Fabry-Perot sensor. The solid-tip sensor utilizes a deformable polymer bubble at the sensor end to react to the applied pressure. The intensity of light reflected by a mirror built onto the end of the polymer tip is modulated by the pressure induced polymer deformations, which is measured by the power meter. The solid-tip sensor is robust and thus can endure rather large intradiscal pressures. However, the inherent difficulties in the fabrication process limit the use of such sensors for intradiscal pressure measurements. The diaphragm based Fabry-Perot pressure sensor utilizes a multi-layered diaphragm that can deform under applied pressures. Such deformations render Fabry-Perot cavity length changes, which can be determined by using the interference fringes obtained from the spectrometer. Repeatable fabrications procedures have been established to produce such sensors, which allow for batch production and controllable sensitivity.

- *In vitro* intradiscal pressure measurements of rodents have been demonstrated with both sensor systems. With the intensity based solid-tip sensor, both displacement controlled and load controlled tests have been performed. In both cases, good correlation between the response and the applied load can be observed. In the case of the low coherence Fabry-Perot sensor system,

calibration experiments have first been carried out, in which the performance properties of the miniature Fabry-Perot sensor and the entire system have been characterized for pressures in the range of 0 psi to 10 psi. The sensitivity of the Fabry-Perot sensor has been determined to be 0.14 µm/psi, with a minimum detectable pressure better than 0.025 psi. With the low coherence Fabry-Perot sensor system, displacement controlled tests for intradiscal pressure measurements have been carried out. The tests show an expected response of an initial drastic increase of pressure due to the applied load, followed by a gradual decay as the disc state neared equilibrium. The results have also revealed that the intradiscal pressures in a rat tail are far higher than 10 psi and a quasi-linear relationship exists between the pressure and the applied load.

5.2 Contributions of the Thesis Research

The contributions of this thesis research can be summarized as follows:

- To the best of the author's knowledge, this is the first attempt to develop miniature fiber optic pressure sensor systems to carry out pressure measurements within rodent discs. Due to the small size of a rodent disc, it is extremely challenging to perform such measurements without disturbing the disc structure. For the first time, rodent disc pressures generated with externally applied loads have been measured; this allows for analysis of the transient response of interstitial fluids, as well as evaluating the discovery of the relationship between the intradiscal pressure and the externally applied load.

- Two types of novel miniature fiber optic pressure sensors have been developed, in which polymer is chosen as the transducer material. Fabrications procedures enabling repeatable construction were established for both fiber optic sensors.

- A Fabry-Perot interferometer utilizing a multi-layered diaphragm design was developed for the first time, allowing for adjustable sensitivity and dynamic range that can be altered during the fabrication process. This allows the sensor to be modified to the specific needs of the application, making it a versatile miniature pressure sensor capable of many uses in addition to intradiscal pressure measurements in rodents. Additionally, the polymer-based diaphragm has good flexibility, enabling a high sensitivity and large dynamic range than the current state-of-the-art miniature Fabry-Perot sensors that use a form of silicon material for the diaphragm.

5.3 Potential Future Work

The research conducted thus far provides a good basis for the study of the biomechanics of the intervertebral disc through *in vitro* intradiscal pressure measurements of rodents. However, there is further research that can be conducted as follows:

- In terms of sensor development, there are some additional issues that can be addressed in a future study. Based on the rodent intradiscal pressure measurements, for a reasonable magnitude of load, it has been found that the pressures in the disc largely exceeded 10 psi, which goes beyond the maximum pressure (10 psi) of the current calibration. For such pressure

levels, larger than expected cavity length changes occur, which indicates that the sensor is still excessively sensitive in the desired pressure range. It will be beneficial to fabricate sensors with thicker diaphragms for this application to obtain a lower sensitivity and a larger dynamic range. Future studies must be conducted to determine the optimum thickness of the sputtering layer and the number of layers of the polymer thin film for the test criteria in the intradiscal pressure measurements of rodents. In addition to improving the sensor performance, it will be helpful to further miniaturize the sensor. The use of the capillary tube with an outer diameter of 363 µm in this research was to keep the sensor as large as possible for easier fabrication while still satisfying the size constraints. Since the outer diameter of the capillary tube is the limiting factor of sensor's size, smaller tubes and thinner fiber (80 µm diameter) can be used to further miniaturize the sensor.

• For the optical system development, a better understanding of the low coherence based Fabry-Perot sensor system must be achieved in the future. It is necessary to develop an optics model of the system to help understand how the mirror properties and the length of the Fabry-Perot cavity influence the visibility and intensity output of the spectrum domain interference fringes. Such an understanding can help achieve an optimal design of the optical system.

• The sensor signal processing can also be improved. Currently, for the low coherence system with a spectrometer to acquire data, the system can only record spectrum data in real time. Then, the data needs to be post-processed

to determine cavity length changes and corresponding pressure values. A truly real time system has not been realized yet due to the limitations of the SpectraSuite software. In a future study, a new data acquisition method, perhaps using LABVIEW, can be developed to visualize the cavity length and corresponding pressure values in real time.

- While the fabrication procedure developed in this research has rendered a miniature sensor that is virtually ready for use in intradiscal pressure measurements, the testing process must be developed further to ensure repeatable and accurate pressure measurements within the intervertebral disc. For example, although the sensor insertion procedures may be adequate, a useful improvement would be a method to determine where the sensor is located in the disc to ensure it has punctured the disc properly and reached the center. If the sensor is inserted too far or not far enough and touches the annulus, the pressure readings can be drastically skewed. To address this, an x-ray guided surgery and insertion process can be pursued; this can potentially enable *in vivo* intradiscal pressure measurements in the future.

Appendix A

This appendix contains the MATLAB codes utilized for spectrum data processing of the low coherence interferometry sensor system.

A1: This is the main program used to post-process the spectrum data from dynamic pressure tests using the high speed acquisition function of the USB4000 spectrometer.

```
%Program: hsa2new
%input: text file directly from the High Speed Acquisition (HSA)
%output: matrix with data point, time, avg cavity, and stdv %
%used to process interference spectrum data from HSA tests


function z = hsa2new(a)

[m, n] = size(a);

increment = 1;      %integration time in seconds (depends on test)
k = 1;              %counter for loop
z = [0, 0, 0, 0];   %becomes output matrix

while k <= (n-1)
    temp = cavity4new(a(:,1),a(:,k+1)); %processes each spectrum
    if temp(1) ~= 0
        z = [z; k, k*increment, temp(1), temp(2)];
    end
    k = k+1;
end

[tempx, tempy] = size(z);
z = z(2:tempx, :, :);               %output matrix

scatter(z(:,2),z(:,3),3,'filled') %graph of the avg cavity vs. time
hold on
xlabel('Time (s)');
ylabel('Cavity Length (um)');
```

A2: This is a function utilized by the code from A1. This function processes the cavity length and standard deviation of a single spectrum. This function is repeatedly used in the program shown in A1 to determine the dynamic changes.

```
%Program: cavity4new
%input: wavelength and intensity of a static test
%output: vector with avg cavity length, stdv %
%used to process single spectrum data from hsa2new program

function a = cavity4new(x,y)

p = findpeaks(x,y,.00002,500,35,35); %peak finder function

[numpeaks,l] = size(p);
k=1;
count=0;


while k<=numpeaks
    if p(k,2)>890
        count = count + 1;
    end
    k = k+1;
end

peaks = p(2:(numpeaks-count),:);
[c,d] = size(peaks);

if c <= 1
    cavity = 0;
else
    [num,f]=size(peaks);
    n=1;
    m=1;
    cavity = 0;
    while n<num
        lamda1=peaks(n,2);
        lamda2=peaks(n+1,2);
        if lamda2-lamda1<=50  %change value depending on idle cavity
            cavity(m)=lamda1*lamda2/(2*(lamda2-lamda1)*1000);
            m = m+1;
        end
        n=n+1;
    end
 end

%cavity = cavity';
avgcavity = mean(cavity);
stdv = std(cavity);
```

```
if avgcavity == 0
    percentage = 0;
else
    percentage = stdv/avgcavity*100;
end

a = [avgcavity percentage];     %output matrix of avg cavity and
stdv %
```

A3: This is a program very similar to the function in A2. This program processes a single spectrum from a static test, displaying a plot of the spectrum and processing the cavity length and standard deviation.

```
%Program: cavity2
%input: text file of single spectrum from USB4000
%output: displays vector with avg cavity length, stdv %
%used to process single spectrum data


function cavity2(a)

x=a(:,1);
y=a(:,2);
p = findpeaks(x,y,.00002,1000,35,35);    %peak finder function

numpeaks = length(p);
k=1;
count=0;

while k<=numpeaks
    if p(k,2)>900
        count = count + 1;
    end
    k = k+1;
end

peaks = p(2:(numpeaks-count),:);

num=length(peaks);
n=1;
cavity = 0;

while n<num
    lamda1=peaks(n,2);
    lamda2=peaks(n+1,2);
    cavity(n)=lamda1*lamda2/(2*(lamda2-lamda1)*1000);
    n=n+1;
end

avgcavity = mean(cavity)
percentage = stdv/avgcavity*100

scatter(peaks(:,2),peaks(:,3))  %spectrum with isolated peaks
hold on
xlabel('Wavelength (nm)');
ylabel('Intensity');
plot(x,y)
```

Appendix B

This appendix contains the plots from additional intradiscal pressure measurement experiments that were briefly mentioned in the thesis.

**B1**: This plot shows the results from a preliminary displacement controlled test of the intervertebral disc. This test gave insight into the required thickness of the diaphragm for the Fabry-Perot interferometer.
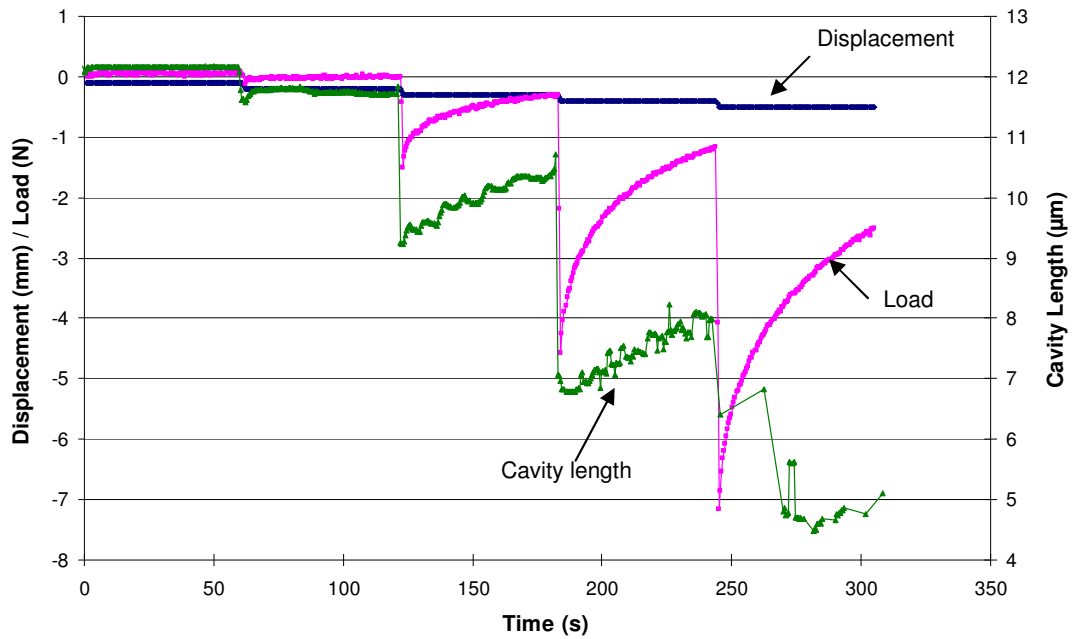
B2: This plot shows the results from the second intradiscal pressure experiment that followed the sensor performance studies. This shows very similar responses to the first intradiscal pressure test in Figure 4.13.
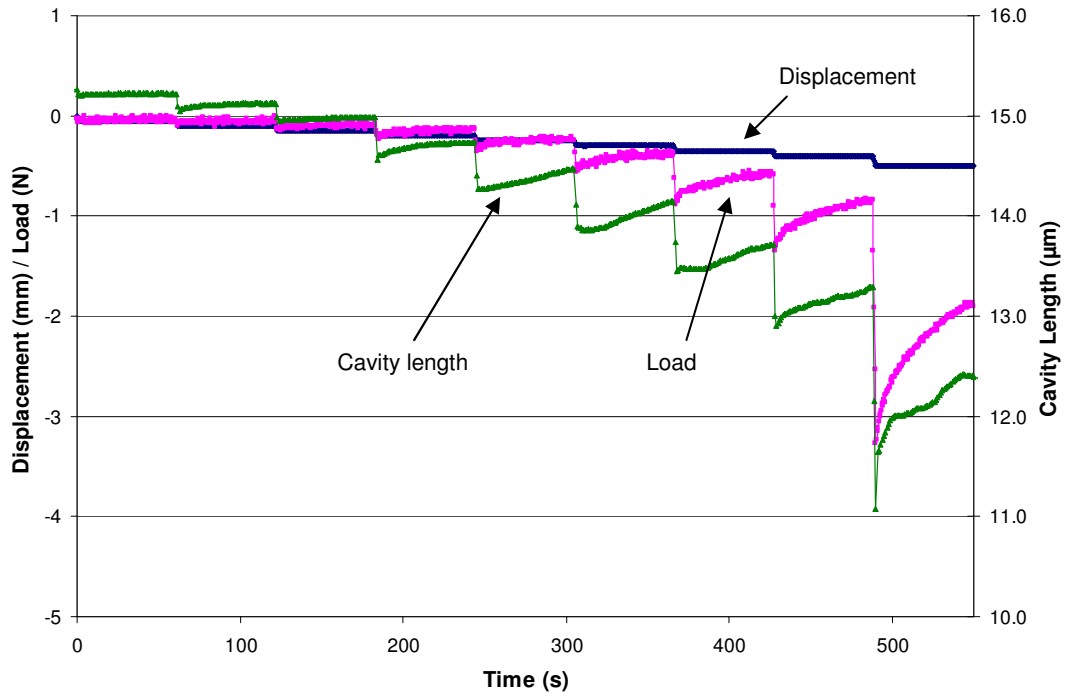
B3: This plot shows the corresponding pressure results below 10 psi from the second intradiscal pressure experiment. This shows very similar responses to the first intradiscal pressure test in Figure 4.14.
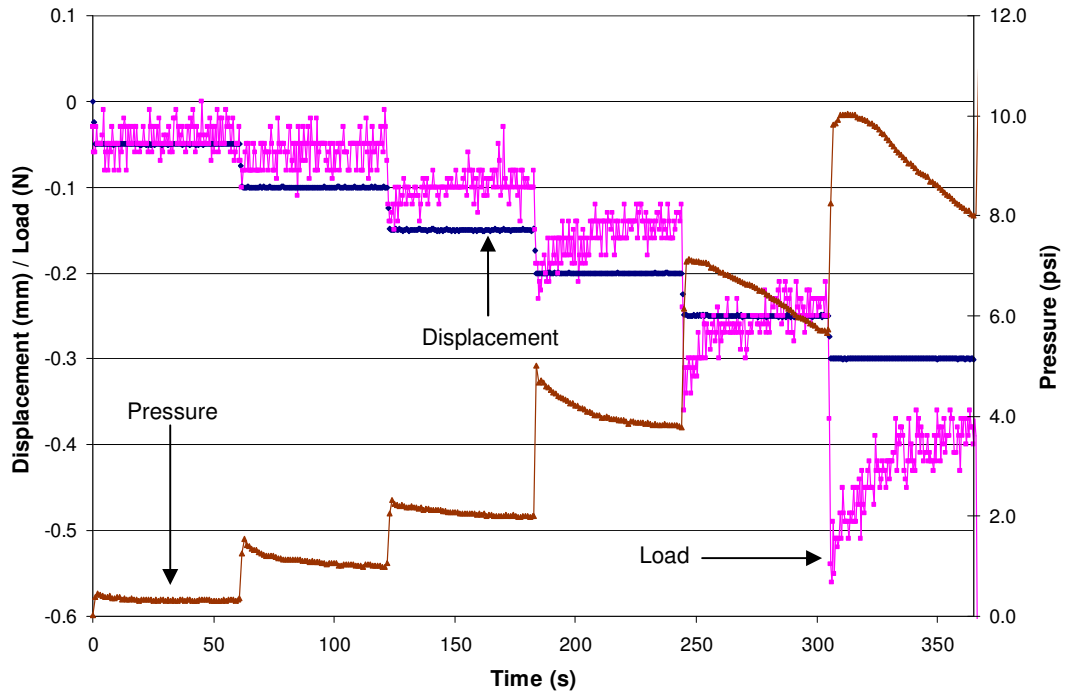
Bibliography

[1]. W.T. Edwards, N.R. Ordway, Y. Zheng, G. McCullen, Z. Han, and H.A. Yuan. "Peak stresses observed in the posterior lateral anulus." *Spine*, 26(16): 1753-1759, 2001.

[2]. H. Wilke, P. Neef, B. Hinz, H. Seidel, and L. Claes. "Intradiscal pressure together with anthropometric data – a data set for the validation of models." *Clinical Biomechanics*, 16, S111-126, 2001.

[3]. J.C. Lotz, O.K. Colliou, J.R. Chin, N.A. Duncan, and E. Liebenberg. "Compression-induced degeneration of the intervertebral disc: an in vivo mouse model and finite-element study." *Spine*. 23(23): 2493-2506, 1998.

[4]. D.J. Polga, B.P. Beaubien, P.M. Kallemeier, K.P. Schellhas, W.D. Lew, G.R. Buttermann, and K.B. Wood. "Measurement of In Vivo Intradiscal Pressure in Healthy Thoracic Intervertebral Discs." *Spine*, 29(12): 1320-1324, 2004.

[5]. T. Guehring, F. UnglaTub, H. Lorenz, G. Omlor, HJ Wilke, and MW Kroeber. "Intradiscal pressure measurements in normal discs, compressed discs and compressed discs treated with axial posterior disc distraction: an experimental study on the rabbit lumbar spine model." *European Spine Journal*, Vol. 15, No. 5, pp. 597-604, 2005.

[6]. L. Ekstrom, S. Holm, A.K. Holm, and T. Hansson, "In vivo porcine intradiscal pressure as a function of external loading." *Journal of Spinal Disord and Techniques*, Vol. 17, No.4, pp. 312-316, 2004.

[7]. D.A. Ryan and A.H. Hsieh. "Viscoelastic behavior of the disc following annular puncture." *American Society of Biomechanics* #179, 2006.

[8]. M. Yu and B. Balachandran, "Acoustic measurements using a fiber optic sensor system." *Journal of Intelligent Material Systems and Structures*, Vol. 14, No.7, pp. 409-414, 2003.

[9]. X. Wang, J. Xu, Y. Zhu, B. Yu, M. Han, K. Cooper, G. Pickrell, and A. Wang, "An optical fiber tip pressure sensor for medical applications." *Conference on Lasers and Electro-Optics / Quantum Electronics and Laser Science Conference (CLEO/QELS)*, Baltimore, May 2005.

[10]. X. Wang, J. Xu, Y. Zhu, K. L. Cooper, and A. Wang, "An all fused silica miniature optical fiber tip pressure sensor." *Optics Letters*, Vol. 31, No. 7, pp. 885-887, 2006.

[11]. Y. Zhu and A. Wang, "Miniature fiber optic pressure sensor." *IEEE Photon. Techn. Lett.*, Vol. 17, No. 2, pp. 447-449, 2005.

[12]. K. Totsu, Y. Haga, and M. Esashi, "Ultra-miniature fiber-optic pressure sensor using white light interferometry." *Journal of Micromechanics and Microengineering*, Vol. 15, No. 1, pp. 71-75, 2005.

[13]. K. Totsu, Y. Haga, and M. Esashi, "Vacuum sealed ultra miniature fiberoptic pressure sensor using white light interferometry," in *12th Int. Conf. Transducers, Solid-State Sensors, Actuators and Microsystems*, Vol. 1, pp. 931–934, 2003.

[14]. W.N. MacPherson, J.M. Kilpatrick, J.S. Barton, and J.D. Jones. "Miniature fiber optic pressure sensors for turbomachinery applications." *Proc. SPIE* Vol. 3478, pp. 283-292, 1998.

[15]. R . Melamud, A.A. Davenport, G.C. Hill, I.H. Chan, F. Declercq, P.G. Hartwell, and B.L. Pruitt. "Development of an SU-8 Fabry-Perot blood pressure sensor." *MEMS 2005. 18th IEEE International Conference*, pp. 810-813, 2005.

[16]. E. Cibula, D. Donlagic, and C. Stropnik. "Miniature Fiber Optic Pressure Sensor for Medical Applications." *Sensors, Proceedings of IEEE,* vol.1, pp. 711- 714, 2002.

[17]. E.S. Olson. "Observing middle and inner ear mechanics with novel intracoclear pressure sensors." *Journal of the Acoustical Society of America*, Vol. 103, Issue 6, pp.3445-3463, 1998.

[18]. J. Dakin and B. Culshaw. *Optical Fiber Sensors: Principals and Components*, Volume 1, Artech, Boston, MA, 1988.

[19]. B. Culshaw and J. Dakin. *Optical Fiber Sensors: Systems and Applications*, Volume 2, Artech, Norwood, MA, 1989.

[20]. Udd, E. *Fiber Optic Sensors: An Introduction for Engineers and Scientists*. New York, NY, Wiley, 1991.

[21]. P.C. Beard, A.M. Hurrell, and T.N. Mills. 2000. "Characterization of a polymer film optical fiber hydrophone for use in the range 1 to 20 MHz: A comparison with PVDF needle and membrane hydrophones," *IEEE Transactions on Ultrasonics, Ferroelectrics, and Frequency Control*, 47(1): pp. 256-265.

[22]. N. Zeng, C. Shi, D. Wang, M. Zhang, and Y. Liao. "Diaphragm-type fiber-optic interferometric acoustic sensor." *Optical Engineering*, Vol. 42(9), pp. 2558-2562, 2003.

[23]. J. Powers. *An Introduction to Fiber Optic Systems*. Homewood, IL, Richard D. Irwin, Inc. and Aksen Associates, Inc, 1993.

[24]. E. Udd. "Fiber optic smart structures." *Proceedings of the IEEE*, Vol.84, Iss.6, pp. 884-894, 1996.

[25]. A.N. Chester, S. Martellucci, and A.M. Verga Scheggi. *Optical Fiber Sensors*. Dordrecht, Martinus Nijhoff Publishers, 1987.

[26]. L. Dai, D. Kelly, J. Pereira, R. Salem, and A. Shooshtari. "Optical Fiber Sensing Network." 31 Oct. 2002. Department of Electrical Engineering, University of MD. 15 May 2006.

[27]. J. Zheng and S. Albin, "Self-referenced reflective intensity modulated fiber-optic displacement sensor." *Optical Engineering*. Vol. 38, pp. 227-232, 1999.

[28]. M. Dagenais, K. Koo, and F. Bucholtz. "Effects of Parasitic Fabry-Perot Cavities In Fiberoptic Interferometric Sensors," *Optics Letters*, Vol. 18(5), pp. 388-390, 1993.

[29]. D.H. Kim, B.Y. Koo, C.G. Kim, and C.S. Hong. "Damage Detection of Composite Structures Using a Stabilized Extrinsic Fabry-Perot Interferometric Sensor System," *Smart Materials and Structures*, Vol. 13(3), pp. 593-598, 2004.

[30]. M. Yu. *Fiber-Optic Sensor Systems for Acoustic Measurements*, Ph.D. Dissertation, University of Maryland, College Park, MD, 2002.

[31]. K.T.V. Grattan and B.T. Meggitt. (1995). *Optical Fiber Sensor Technology*. London, Chapman & Hall.

[32]. K.T.V. Grattan and B.T. Meggitt. (1999). *Optical fiber Sensor Technology Volume 4; Chemical and Environmental Sensing*. London, Kluwer Academic Publishers

[33]. "HL2000 Tungsten Halogen Light Sources." *Ocean Optics Inc*. August 2006. 8, September 2006. <http://www.oceanoptics.com/products/hl2000.asp>

[34]. "Grating Efficiency Curves." *Ocean Optics Inc*. August 2006. 8, September 2006. <http://www.oceanoptics.com/technical/gratingcharts.asp#5-9>

[35]. J. Xu. *High Temperature High Bandwidth Fiber Optic Pressure Sensors*, Ph.D. Dissertation, Virginia Polytechnic Institute and State University , Blacksburg, VA, 2005.

[36]. M. Li, M. Wang, and H. Li. "Optical MEMS pressure sensor based on Fabry-Perot interferometry" *Optics Express*, Vol. 14, Iss. 4, pp. 1497-1504, 2006.

[37]. L.L. Lapin. *Probability and Statistics for Modern Engineering*. Boston, PWS-
KENT Publishing Company, 1990.